

An updated nuclear-physics and multi-messenger astrophysics framework for binary neutron star mergers

Peter T. H. Pang^{1,2}, Tim Dietrich^{3,4,*}, Michael W. Coughlin⁵, Mattia Bulla^{6,7,8,9}, Ingo Tews¹⁰, Mouza Almualla¹¹, Tyler Barna⁵, Ramodgwendé Weizmann Kiendrebeogo^{12,13}, Nina Kunert³, Gargi Mansingh^{5,14}, Brandon Reed^{5,15}, Niharika Sravan¹⁶, Andrew Toivonen⁵, Sarah Antier¹³, Robert O. VandenBerg⁵, Jack Heinzel¹⁷, Vsevolod Nedora⁴, Pouyan Salehi³, Ritwik Sharma¹⁸, Rahul Somasundaram^{10,19,20}, Chris Van Den Broeck^{1,2}

¹Nikhef, Science Park 105, 1098 XG Amsterdam, The Netherlands ²Institute for Gravitational and Subatomic Physics (GRASP), Utrecht University, Princetonplein 1, 3584 CC Utrecht, The Netherlands ³Institut für Physik und Astronomie, Universität Potsdam, Haus 28, Karl-Liebknecht-Str. 24/25, 14476, Potsdam, Germany ⁴Max Planck Institute for Gravitational Physics (Albert Einstein Institute), Am Mühlenberg 1, Potsdam 14476, Germany ⁵School of Physics and Astronomy, University of Minnesota, Minneapolis, Minnesota 55455, USA ⁶The Oskar Klein Centre, Department of Astronomy, Stockholm University, AlbaNova, SE-106 91 Stockholm, Sweden ⁷Department of Physics and Earth Science, University of Ferrara, via Saragat 1, I-44122 Ferrara, Italy ⁸INFN, Sezione di Ferrara, via Saragat 1, I-44122 Ferrara, Italy ⁹INAF, Osservatorio Astronomico d'Abruzzo, via Mentore Maggini snc, 64100 Teramo, Italy ¹⁰Theoretical Division, Los Alamos National Laboratory, Los Alamos, NM 87545, USA ¹¹Department of Physics, American University of Sharjah, PO Box 26666, Sharjah, UAE ¹²Laboratoire de Physique et de Chimie de l'Environnement, Université Joseph Kl-ZERBO, Ouagadougou, Burkina Faso ¹³Observatoire de la Côte d'Azur, Université Côte d'Azur, CNRS, 96 boulevard de l'observatoire, F06304 Nice cedex 4, France ¹⁴Department of Physics, American University, Washington, DC 20016, USA. ¹⁵Department of Physics and Astronomy, University of Minnesota – Duluth, Duluth, MN 55812 ¹⁶Department of Physics, Drexel University, Philadelphia, PA 19104, USA ¹⁷Department of Physics, Massachusetts Institute of Technology, 77 Massachusetts Ave, Cambridge, MA 02139, USA. ¹⁸Department of Physics, Deshbandhu College, University of Delhi, New Delhi, India. ¹⁹Univ Lyon, Univ Claude Bernard Lyon 1, CNRS/IN2P3, IP2I Lyon, UMR 5822, F-69622, Villeurbanne, France ²⁰Department of Physics, Syracuse University, Syracuse, NY 13244, USA *tim.dietrich@uni-potsdam.de

Abstract

The multi-messenger detection of the gravitational-wave signal GW170817, the corresponding kilonova AT2017gfo and the short gamma-ray burst GRB170817A, as well as the observed afterglow has delivered a scientific breakthrough. For an accurate interpretation of all these different messengers, one requires robust theoretical models that describe the emitted gravitational-wave, the electromagnetic emission, and dense matter reliably. In addition, one needs efficient and accurate computational tools to ensure a correct cross-correlation between the models and the observational data. For this purpose, we have developed the Nuclear-physics and Multi-Messenger Astrophysics framework NMMA. The code allows incorporation of nuclear-physics constraints at low densities as well as X-ray and radio observations of isolated neutron stars. In previous works, the NMMA code has allowed us to constrain the equation of state of supranuclear dense matter, to measure the Hubble constant, and to compare dense-matter physics probed in neutron-star mergers and in heavy-ion collisions, and to classify electromagnetic observations and perform model selection.

Here, we show an extension of the NMMA code as a first attempt of analysing the gravitational-wave signal, the kilonova, and the gamma-ray burst afterglow simultaneously. Incorporating all available information, we estimate the radius of a $1.4M_{\odot}$ neutron star to be $R = 11.98^{+0.35}_{-0.40}$ km.

1 Introduction

The study of the gravitational-wave (GW) and electromagnetic (EM) signals GW170817¹, AT2017gfo^{2–12}, and GRB170817A^{13–15} has already enabled numerous scientific breakthroughs, for example, constraints on the properties of neutron stars (NSs) and the dense matter equation of state (EOS) at supranuclear densities^{16–23}, an independent measurement of the Hubble constant^{22,24–28}, the verified connection between binary NS (BNS) mergers and at least some of the observed short gamma-ray bursts (GRBs)²⁹, and precise limits on the propagation speed of GWs²⁹. These scientific achievements were enabled by the multi-messenger nature of GW170817.

Despite this enormous progress, results have been obtained by connecting constraints from individual messengers a posteriori, i.e., different messengers were analyzed individually and then combined within different multi-messenger frameworks to achieve the final results. Such frameworks and attempts include, among others, the work of Breschi et al.³⁰ performing Bayesian inference and model selection on the kilonova AT2017gfo, Nicholl et al.³¹ developing a framework for predicting kilonova and GRB afterglow lightcurves using information from GW signals as input, and the multi-messenger framework developed by Raaijmakers et al.³². Similarly, to these works, our previous Nuclear physics - Multi-Messenger Astrophysics (NMMA) framework has been successfully applied to provide constraints on the EOS of NS matter and on the Hubble constant^{22,33}, to investigate the nature of the compact binary merger GW190814³⁴, to provide techniques to search for kilonova transients³⁵, to classify observed EM transients such as GRB200826A³⁶, and to combine information from multi-messenger observations with data from nuclear-physics experiments such as heavy-ion collisions²³.

Here, we upgrade our framework to allow for a simultaneous analysis of kilonova, GRB afterglow, and GW data capitalizing on the multi-messenger nature of compact-binary mergers.

2 Results

The full potential of our NMMA study becomes clear from Fig. 1 where we show a set of possible EOSs relating the pressure and baryon number density inside NSs. Different constraints can provide valuable information in different density regimes. For example, theoretical calculations of dense nuclear matter in the framework of chiral effective field theory (EFT)^{39–43} or data extracted from

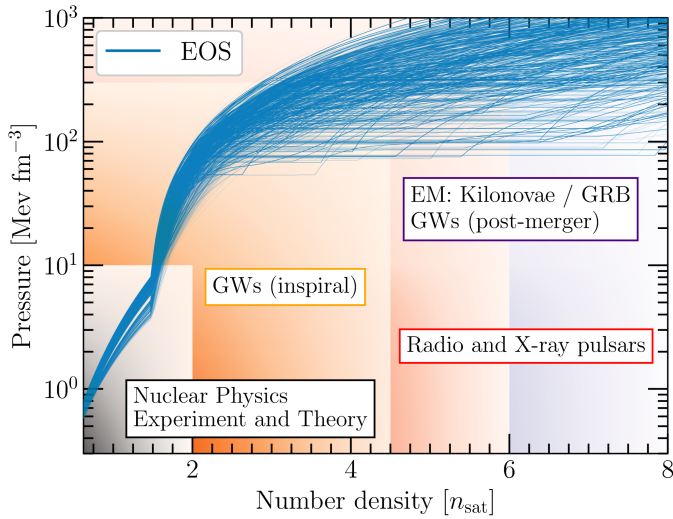


Figure 1 | Overview of constraints on the EOS from different information channels. We show a set of possible EOSs (blue lines) that are constrained up to $1.5n_{\text{sat}}$ by Quantum Monte Carlo calculations using chiral EFT interactions³⁷ and extended to higher densities using a speed of sound model³⁸. Different regions of the EOS can then be constrained by using different astrophysical messengers, indicated by rectangles: GWs from inspirals of a BNS or black-hole–NS (BHNS) systems contain information that probe the EOS at densities realized inside the individual NS components of the system, typically up to about five times n_{sat} , but the exact density range probed in such mergers depends noticeably on the mass of the component stars. Furthermore, radio observations of NSs can be used to infer their masses, e.g., by measuring Shapiro delay in a binary system. In particular, radio observations of heavy NSs with masses of about $2M_{\odot}$, such as PSR J0348+0432⁴⁶, PSR J1614-2230⁴⁷, and PSR J0740+6620⁴⁸, currently provide valuable information at larger densities than those probed by inspiral GW signals. In addition, these observations provide a valuable lower bound on the maximum mass of NSs. Matter at the highest densities in the universe could be created in the postmerger phase of a BNS coalescence, i.e., after the collision of the two NSs in the binary. This phase of the binary merger might be observed through future GW detections with more sensitive detectors. Alternatively, this phase can be probed by analyzing EM signals connected to a BNS merger, i.e., the kilonovae, GRBs, and their afterglows. Finally, at asymptotically high densities that are not shown in the figure, the EOSs can be calculated in perturbative QCD⁴⁹ and might be used to constrain the NS EOS⁵⁰. The combination of all these various pieces of information provides a unique tool to unravel the properties of matter at supranuclear densities.

nuclear-physics experiments, e.g., heavy-ion collisions⁴⁴ or the recent PREX-II experiment at Jefferson Laboratory⁴⁵, provide valuable input up to about twice the nuclear saturation density, $n_{\text{sat}} \approx 0.16 \text{ fm}^{-3}$. GW signals emitted during the inspiral of a BNS or black-hole–NS (BHNS) systems contain information that probe the EOS at densities realized inside the individual NS components of the system, typically up to about five times n_{sat} , but the exact density range probed in such mergers depends noticeably on the mass of the component stars. Furthermore, radio observations of NSs can be used to infer their masses, e.g., by measuring Shapiro delay in a binary system. In particular, radio observations of heavy NSs with masses of about $2M_{\odot}$, such as PSR J0348+0432⁴⁶, PSR J1614-2230⁴⁷, and PSR J0740+6620⁴⁸, currently provide valuable information at larger densities than those probed by inspiral GW signals. In addition, these observations provide a valuable lower bound on the maximum mass of NSs. Matter at the highest densities in the universe could be created in the postmerger phase of a BNS coalescence, i.e., after the collision of the two NSs in the binary. This phase of the binary merger might be observed through future GW detections with more sensitive detectors. Alternatively, this phase can be probed by analyzing EM signals connected to a BNS merger, i.e., the kilonovae, GRBs, and their afterglows. Finally, at asymptotically high densities that are not shown in the figure, the EOSs can be calculated in perturbative QCD⁴⁹ and might be used to constrain the NS EOS⁵⁰. The combination of all these various pieces of information provides a unique tool to unravel the properties of matter at supranuclear densities.

GW170817-AT2017gfo

With the NMMA framework, we analyze GW170817 simultaneously with the observed kilonova AT2017gfo. For the GW analysis, we have used the IMRPhenomPv2.NRTidalv2 waveform model and analyzed the GW data obtained from the Gravitational Wave Open Science Center (GWOSC)⁵¹ in a frequency range of 20Hz to 2048Hz, covering the detected BNS inspiral⁵². For the EM signal, we use the data

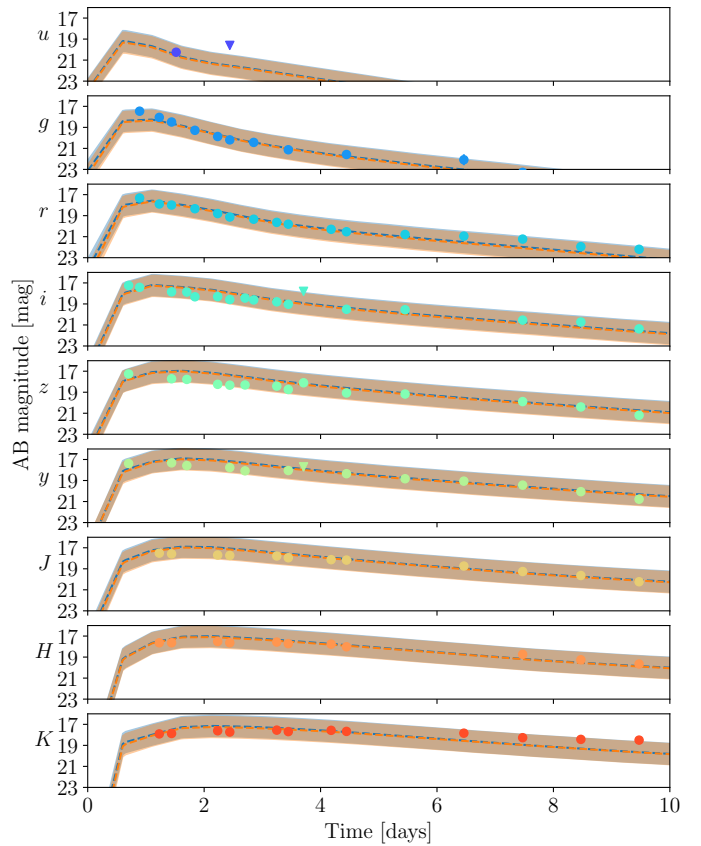


Figure 2 | Best-fit early-time lightcurve from the analysis. The best-fit lightcurves (dashed, with the 1 magnitude uncertainty shown as the band) for AT2017gfo data when analysing GW170817-and-AT2017gfo (orange) or GW170817-and-AT2017gfo-and-GRB170817A (blue) simultaneously. We note that both bands overlap almost completely, i.e., for AT2017gfo the accuracy of the kilonova lightcurve description does not depend noticeably on the inclusion of a GRB afterglow component. For the analysis, we restrict our dataset to times between 0.5 days up to 10 days after the BNS merger to simplify the joint GW170817-and-AT2017gfo-and-GRB170817A study as discussed in the main text.

set compiled in Coughlin et al.⁵³, where in this work, we include the optical, infrared, and ultraviolet data between 0.5 and 10 days after the merger. The corresponding data is analysed with a Gaussian Process Regression (GPR)-based kilonova model. For our analysis, we are presenting the best-fit lightcurve in Fig. 2, with its band representing a one magnitude uncertainty for the individual lightcurves. This one magnitude uncertainty is introduced during the inference and should account for systematic uncertainties in kilonova modelling. In Supplementary information, we show how smaller or larger assumed uncertainties change our conclusions and it show that the one-magnitude is a sensible choice. Such a finding is also consistent with Heinzl et al.⁵⁴. Therefore, we focus particularly on one-magnitude uncertainties’ results. Nevertheless further work would be needed to understand in detail uncertainties related to the ejecta geometry⁵⁴, assumed heating rates, thermalization efficiencies and opacities within the ejecta⁵⁵. Furthermore, we point out that for Fig. 2, we explicitly restricted our data set to the times between 0.5 to 10 days after the BNS merger, since model predictions at earlier or later times are more uncertain, e.g., due to less accurate opacities during early times and a larger impact of Monte Carlo noise in the employed radiative transfer models at late times. While this does not affect the GW170817-AT2017gfo analysis, it has an impact when we will also incorporate the GRB af-

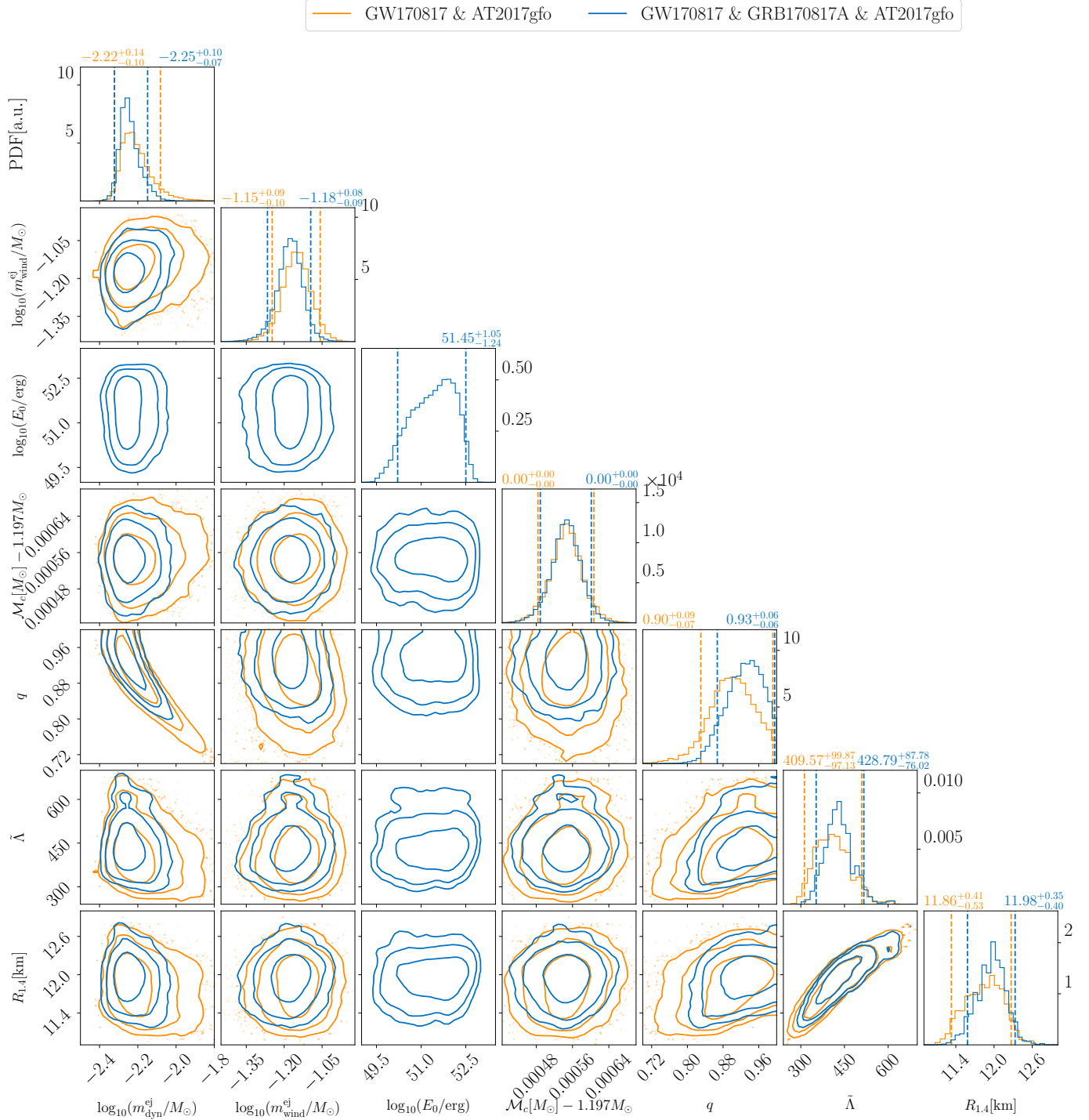


Figure 3 | Visualization of the posterior of the GW170817-and-AT2017gfo and GW170817-and-AT2017gfo-and-GRB170817A analysis. Corner plot for the mass of the dynamical ejecta $m_{\text{dyn}}^{\text{ej}}$, the mass of the disk wind ejecta $m_{\text{wind}}^{\text{ej}}$, \log_{10} of the GRB jet on-axis isotropic energy $\log_{10} E_0$, the detector-frame chirp mass \mathcal{M}_c , the mass ratio q , the mass-weighted tidal deformability $\tilde{\Lambda}$, and the radius of a 1.4 solar mass neutron star $R_{1.4}$ at 68%, 95% and 99% confidence. For the 1D posterior probability distributions, we mark the median (solid lines) and the 90% confidence interval (dashed lines) and report these above each panel. We show results that are based on the simultaneous analysis of GW170817-and-AT2017gfo (orange) and of GW170817-and-AT2017gfo-and-GRB170817A (blue).

terglow. In fact, we find that not restricting us to this time ranges can cause problems in the joint inference and it takes noticeably longer until the sampler converges.

Fig. 3 summarizes our main findings and shows joint posteriors for the mass of the dynamical ejecta $m_{\text{dyn}}^{\text{ej}}$, the mass of the disk wind ejecta $m_{\text{wind}}^{\text{ej}}$, the chirp mass \mathcal{M}_c , the mass ratio q , the mass-weighted tidal deformability $\bar{\Lambda}$, and the radius of a 1.4 solar mass neutron star $R_{1.4}$. In contrast to previous findings using simpler kilonova modelling (see Ref. 56 and references therein), we can fit AT2017gfo with masses for the dynamical (about $0.006 M_{\odot}$) and disk-wind (about $0.07 M_{\odot}$) ejecta components that are within the range of values predicted by numerical-relativity simulations⁵⁷. While the parameters extracted are consistent with our previous findings²², we observe a clear improvement on the parameter error bounds due to (i) performing a simultaneous analysis of the distinct messengers and (ii) employing a modified likelihood function when analysing the kilonova. For instance, the constraints on $R_{1.4} = 11.86^{+0.41}_{-0.53}$, a typical choice to quantify EOS constraints, is significantly improved compared to our previous result, $R_{1.4} = 11.75^{+0.86}_{-0.81}$ km²². The half-width of $R_{1.4}$'s 90% credible interval decreases from about 800m²² to about 400m.

GW170817-AT2017gfo-GRB170817A

In addition to the combined analysis of GW170817 and AT2017gfo, we can also incorporate information obtained from the GRB afterglow of GW170817A, where we employ the data set collected in Troja et al.⁵⁸. The GRB afterglow light-curve data are analyzed with the synthetic Gaussian jet-model lightcurve described before^{59,60}. Fig. 2 shows the corresponding best-fit lightcurve for the kilonova with a 1 magnitude uncertainty band as before. Moreover, we are also presenting the best-fit lightcurve, which includes kilonova and GRB afterglow, and the employed uncertainty band in Fig. 4. We find that both the kilonova AT2017gfo and the GRB afterglow GRB170817A are well described in our analysis.

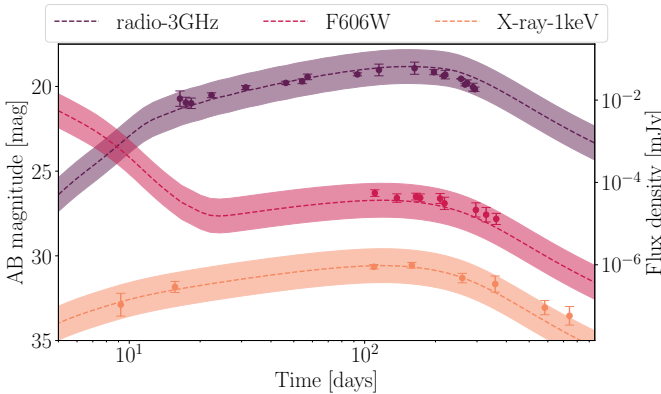


Figure 4 | Best-fit late-time lightcurve from the analysis. The best-fit lightcurves (dashed, with the 1 magnitude uncertainty shown as the band) for the analysis of GRB170817A when simultaneously analysing GW170817, AT2017gfo, GRB170817A. We compare our model predictions with the observational data including the 1-sigma measurement uncertainty.

Fig. 3 again summarizes our findings for the joint posteriors of the mass of the dynamical ejecta, the mass of the disk wind ejecta, the on-axis isotropic equivalent energy, the chirp mass, the mass ratio, the mass-weighted tidal deformability, and the radius of a 1.4 solar mass neutron star for this analysis, which is consistent with GW170817-and-AT2017gfo only. Compared to the analysis of GW170817-and-AT2017gfo only, the improvement on the parameter uncertainties is minimal, yet, noticeable when information from GRB170817A is added. Although no significant constraint on the EOS is imposed by

the jet energy E_0 as the ratio ξ between it, E_0 , and the disk mass m_{disk} is taken as a free parameter, the inclination constraint from the GRB plays a role in the constraint on EOS. For an anisotropic kilonova model, the inclination angle changes the observable kilonova light curves beyond scaling (e.g. Fig. 2 in Ref. 61), which is correlated with the ejecta masses (e.g. Fig. 3 in Ref. 62). Therefore the GRB's inclination measurement imposes a constraint on the EOS via the kilonova eject masses measurements.

Moreover, for future studies, we expect that the inclusion of the GRB afterglow will be of great importance for measuring the Hubble constant.

3 Discussion

We have developed a publicly available NMMA framework for the interpretation and analysis of BNS and BHNS systems. This framework allows for the simultaneous analysis of GW and EM signals such as kilonovae and GRB afterglows. In addition, our framework allows us to incorporate constraints from nuclear-physics calculations, e.g., by sampling over EOS sets constrained by chiral EFT, and to include radio as well as X-ray measurements of isolated NSs. By employing our framework to a combined analysis of GW170817, AT2017gfo, and GRB170817A, we find that the radius of a typical 1.4 solar mass NS lies within $11.98^{+0.35}_{-0.40}$ km; cf. Tab. 1 for a selection of studies from the literature. Based on our findings, our analysis is a noticeable improvement over previous works. However, additional uncertainties in our work lie in limited physics input in kilonova and semi-analytic GRB and models. Therefore, reliable astrophysical interpretations of future BNS detections will only be possible if not only parameter estimation infrastructure, as presented in this work, but also the astrophysical models describing transient phenomena advance further. Nevertheless, given the increasing number of multi-messenger detections of BNS and BHNS merger, we expect to use our framework to further increase our knowledge about the interior of NSs during the coming years.

Table 1 | Comparison of radius measurements of a $1.4M_{\odot}$ neutron star for a selection of multi-messenger studies.

Reference	$R_{1.4}$ [km]
Dietrich et al. ²²	$11.75^{+0.86}_{-0.81}$ (90%)
Essick et al. ⁶³	$12.54^{+0.71}_{-0.63}$ (90%)
Breschi et al. ³⁰	$11.99^{+0.82}_{-0.85}$ (90%)
Nicholl et al. ³¹	$11.06^{+1.01}_{-0.98}$ (90%)
Raaijmakers et al. ⁶⁴	$12.18^{+0.56}_{-0.79}$ (95%)
Miller et al. ⁶⁵	$12.45^{+0.65}_{-0.65}$ (68%)
Huth et al. ²³	$12.01^{+0.78}_{-0.77}$ (90%)
this work [NMMA]	$11.98^{+0.35}_{-0.40}$ (90%)

A selected list of radius measurements of a $1.4M_{\odot}$ neutron star from various multi-messenger studies is shown. We denote the corresponding credible interval in parenthesis.

4 Methods

Equation of State construction

The EOS describes the relation between energy density ε , pressure p , and temperature T of dense matter and additionally depends on the composition of the system. For NSs, thermal energies are much smaller than typical Fermi energies of the particles, and therefore, temperature effects can be neglected for isolated NSs or NSs in the inspiral phase of a merger. In these cases, the EOS simply relates ε and p .

The most general constraints on the EOS can be inferred from the

slope of the EOS, the speed of sound, defined as

$$c_S = c\sqrt{\partial p/\partial \varepsilon}, \quad (1)$$

where c is the speed of light. Due to the laws of special relativity, the speed of sound has to be smaller than the speed of light, $c_S \leq c$. Furthermore, the speed of sound in a NS has to be larger than zero, $c_S \geq 0$, as NSs would otherwise be unstable. These constraints alone, however, allow for an extremely large EOS space.

At nuclear densities, additional information on the EOS can be inferred from laboratory experiments and theoretical nuclear-physics calculations. For example, this information was used to constrain the properties of stellar matter in the NS crust^{66,67}, i.e., the outermost layer of NSs at densities below approximately $0.5n_{\text{sat}}$. Above roughly $0.5n_{\text{sat}}$, NS matter consists of a fluid of neutrons with a small admixture of protons. In this regime, the EOS can be constrained by microscopic calculations of dense nuclear matter. These calculations typically provide the energy per particle, $E/A(n, x)$, which is a function of density n and proton fraction $x = n_p/n$ with n_p being the proton density. From this, the EOS follows from

$$\varepsilon(n, x) = n \frac{E}{A}(n, x), \quad (2)$$

and

$$p(n, x) = n^2 \frac{\partial E/A(n, x)}{\partial n}. \quad (3)$$

The proton fraction $x(n)$ is then determined from the beta equilibrium condition, $\mu_n = \mu_p + \mu_e$, where μ_i is the chemical potential of particle species i , and n , p , and e refer to neutrons, protons, and electrons, respectively.

To calculate the energy per particle microscopically, one needs to solve the nuclear many-body problem, commonly described by the Schrödinger equation. This requires knowledge of the nuclear Hamiltonian describing the many-body system. Fundamentally, nuclear many-body systems are described by Quantum Chromodynamics (QCD), the fundamental theory of strong nuclear interactions. QCD describes the system in terms of the fundamental degrees of freedom (d.o.f.), quarks and gluons. Unfortunately, this approach is currently not feasible⁶⁸. At densities of the order of n_{sat} , however, the effective d.o.f. are nucleons, neutrons and protons, that can be treated as point-like nonrelativistic particles. Then, the nuclear Hamiltonian can be written generically as

$$H = T + \sum_{i < j} V_{ij}^{\text{NN}} + \sum_{i < j < k} V_{ijk}^{\text{3N}} + \dots, \quad (4)$$

where T denotes the kinetic energy of the nucleons, V_{ij}^{NN} describes two-nucleon (NN) interactions between nucleons i and j , and V_{ijk}^{3N} describes three-nucleon (3N) interactions between nucleons i , j , and k . In principle, interactions involving four or more nucleons can be included, but initial studies have found these to be small compared to present uncertainties⁶⁹.

The derivation of the nuclear Hamiltonian (Eq. (4)) from QCD is not feasible due to its nonperturbative nature. In this work, we therefore use a common approach and choose nucleons as effective d.o.f. The interactions among nucleons can then be derived in the framework of Chiral Effective Field Theory (EFT)^{70,71}. Chiral EFT starts out with the most general Lagrangian consistent with all the symmetries of QCD in terms of nucleonic degrees of freedom. It explicitly includes meson-exchange interactions for the lightest mesons, i.e., the pions. This approach yields an infinite number of pion-exchange and nucleon-contact interactions which needs to be organized in terms of a hierarchical expansion in powers of a soft (low-energy) scale over a hard (high-energy) scale. In chiral EFT, the soft scale q is given by the nucleons' external momenta or the pion mass. The hard scale, also called the breakdown scale Λ_b , is of the order of 500 – 600 MeV⁷² and

interaction contributions involving heavier d.o.f., such as the ρ meson, are integrated out. The chiral Lagrangian is then expanded in powers of q/Λ_b according to a power-counting scheme. Most current chiral EFT interactions are derived in Weinberg power counting^{70,71,73–75}. One can then derive the nuclear Hamiltonian from this chiral Lagrangian in a consistent order-by-order framework that allows for an estimate of the theoretical uncertainties^{72,76,77} and that can be systematically improved by increasing the order of the calculation. Chiral EFT Hamiltonian naturally include NN, 3N, and higher many-body forces, see Eq. (4), and chiral EFT predicts a natural hierarchy of these contributions. For example, 3N interactions start to contribute at third order ($N^2\text{LO}$) in the expansion. Typical state-of-the-art calculations truncate the chiral expansion at $N^2\text{LO}$ ^{39,42,78} or fourth order ($N^3\text{LO}$)^{41,79}.

With the nuclear Hamiltonian at hand, one then needs to solve the many-body Schrödinger equation which requires advanced numerical methods. Examples of such many-body techniques include many-body perturbation theory (MBPT)^{40,41,79}, the self-consistent Green's function (SCGF) method⁸⁰, or the coupled-cluster (CC) method^{78,81}. Here, we employ Quantum Monte Carlo (QMC) methods⁸², which provide nonperturbative solutions of the Schrödinger equation. QMC methods are stochastic techniques which treat the Schrödinger equation as a diffusion equation in imaginary time. In the QMC framework, one begins by choosing a trial wavefunction of the many-body system, which for nuclear matter can be described as a Slater determinant of non-interacting fermions multiplied with NN and 3N correlation functions. This trial wavefunction is evolved to large imaginary times, projecting out high-energy excitations, and converging to the true ground state of the system as long as the trial wavefunction has a non-zero overlap with it. Among QMC methods, two well-established algorithms are Green's function Monte Carlo (GFMC), used to describe light atomic nuclei with great precision⁸², and Auxiliary Field Diffusion Monte Carlo (AFDMC)⁸³, suitable to study larger systems such as nuclear matter. Here, we employ AFDMC calculations of neutron matter but our NMMA framework is sufficiently flexible to employ any low-density calculation for neutron-star matter. We then extend our neutron-matter calculations to neutron-star conditions by extrapolating the calculations to β equilibrium using phenomenological information on symmetric nuclear matter and constructing a consistent crust reflecting the uncertainties of the calculations⁸⁴. This crust includes a description of the outer crust⁶⁶ and uses the Wigner-Seitz approximation to calculate the inner-crust EOS consistently with our AFDMC calculations.

At nuclear densities, chiral EFT together with a suitable many-body framework provides for a reliable description of nuclear matter with systematic uncertainty estimates. With increasing density, however, the associated theoretical uncertainty grows fast due to the correspondingly larger nucleon momenta approaching the breakdown scale. The density up to which chiral EFT remains valid is not exactly known but estimates place it around $2n_{\text{sat}}$ ^{37,72}. Hence, chiral EFT calculations constrain the EOS only up to these densities but to explore the large EOS space beyond the breakdown of chiral EFT, one requires a physics-agnostic extension scheme. Here, physics-agnostic implies that no model assumptions, e.g., about the existence of certain d.o.f. at high densities, are made. Instead, the EOS is only bounded by conditions of causality, $c_S \leq c$, and mechanical stability, $c_S \geq 0$, mentioned before. There exist several such extension schemes in literature: parametric ones, like the polytropic expansion^{85–87} or expansions in the speed of sound^{88,89}, and nonparametric approaches⁹⁰. To extend the AFDMC calculations employed here, we employ a parametric speed-of-sound extension scheme. Working in the c_S versus n plane, the speed of sound $c_S(n)$ is determined with theoretical uncertainty estimates by chiral EFT up to a reference density below the expected breakdown density. From this uncertainty band, we sample a speed-of-sound curve up to the reference density. Beyond this density,

we create a typically non-uniform grid in density up to a large density $\approx 12n_{\text{sat}}$, well beyond the regime realized in NSs. For each grid point, we sample random values for $c_s^2(n_i)$ between 0 and c^2 (we set $c = 1$ in the following). We then connect the chiral EFT draw for the speed of sound with all points $c_{s,i}^2(n_i)$ using linear segments. The resulting density-dependent speed of sound can be integrated to give the EOS, i.e., the pressure, baryon density, and energy density. In the interval $n_i \leq n \leq n_{i+1}$,

$$p(n) = p(n_i) + \int_{n_i}^n c_s^2(n') \mu(n') dn', \quad (5)$$

$$\epsilon(n) = \epsilon(n_i) + \int_{n_i}^n \mu(n') dn', \quad (6)$$

where $\mu(n)$ is the chemical potential that can be obtained from the speed of sound using the relation

$$\mu(n) = \mu_i \exp \left[\int_{\log n_i}^{\log n} c_s^2(\log n') d \log n' \right]. \quad (7)$$

For each reconstructed EOS, constrained by Chiral EFT at low densities and extrapolated via the c_S extension to larger densities, the global properties of NSs can be calculated by solving the Tolman–Oppenheimer–Volkoff (TOV) equations. This way, we determine the NS radii (R) and dimensionless tidal deformabilities (Λ) as functions of their masses (M). We repeat this approach for a large number of samples to construct EOS priors for further analyses of NS data.

This approach is flexible and additional information on high-density phases of QCD can be included straightforwardly. For example, pQCD calculations at asymptotically high densities⁴⁹, of the order of $40 - 50n_{\text{sat}}$, might be used to constrain the general EOS extension schemes even further^{50,87}. However, the exact impact of these constraints at densities well beyond the regime realized in NSs needs to be studied in more detail. While our NMMA framework currently does not have this capability, we are planning to add this in the near future. Similarly, instead of using general extension models, one can employ specific high-density models accounting for quark and gluon d.o.f. One such model is the quarkyonic-matter model^{91–94}, which describes the observed behavior of the speed of sound in NSs³⁷: a rise of the speed of sound at low densities to values above the conformal limit of $c/\sqrt{3}$, followed by a decrease to values below the conformal limit at higher densities. In future work, we will address quarkyonic matter and other models in our NMMA framework.

The construction of the EOS, as detailed above, is implemented in the NMMA code under the class `EOS_with_CSE`. This class allows for (a) an exploration of theoretical uncertainties in the low-density EOS and (b) constructs the high-density EOS using a c_S extrapolation. (a) Low-density uncertainties are implemented by requiring two tabulated EOS files for the lower and upper bound of the uncertainty band as inputs, containing the pressure, energy density and number density up to the chosen breakdown density of the model. By default, the results of a QMC calculation using local chiral EFT interactions at N²LO³⁷ with theoretical uncertainties are provided. Upon initiation of the class, a sample is drawn from the low-density uncertainty band using a 1-parameter sampling technique. In this approach, a uniform random number ω is sampled uniformly between 0 and 1, and the interpolated EOS is given as

$$p(n) = p_{\text{soft}}(n) + \omega(p_{\text{stiff}}(n) - p_{\text{soft}}(n)), \quad (8)$$

$$\epsilon(n) = \epsilon_{\text{soft}}(n) + \omega(\epsilon_{\text{stiff}}(n) - \epsilon_{\text{soft}}(n)), \quad (9)$$

where the subscripts “soft” and “stiff” refer to the lower and upper bounds of the EFT uncertainty band, respectively. This sampling technique assumes that pressure and energy density are correlated but we have found that releasing this assumption and using a four-parameter

form suggested by Gandolfi et al.⁹⁵ does not change our results appreciably. In future, we will explore additional schemes, e.g., using Gaussian processes⁶³.

(b) The EOS given by Eqs. (8) and (9) is used up to a breakdown density determined by the user. By default, this density is set to $2n_{\text{sat}}$. Beyond this density, the class constructs the EOS using a c_S extension. The maximum density up to which the EOS is extrapolated and the number of linear line segments can be adjusted by the user, with the default values being $12n_{\text{sat}}$ for the former and 5 line segments for the latter. The code then solves Eqs. (5), (6) and (7) to give the extrapolated EOS. The pressure, energy density, and number density describing the full EOS are accessible as attributes of the `EOS_with_CSE` class.

Finally, the method `construct_family` solves the stellar structure equations (TOV equations and equations for the quadrupole perturbation of spherical models), and returns a sequence of NSs with their masses, radii and dimensionless tidal deformabilities as arrays.

Prior weighting to incorporate radio and X-ray observations of single neutron stars

To incorporate mass measurements of heavy pulsars and mass-radius measurements of isolated pulsars, the associated likelihood is calculated and taken as the prior probability for an EOS for further analysis. For instance, the radio observations on PSR J0348+4042⁴⁶, and PSR J1614-2230⁴⁷ provide a lower bound on the maximum mass of a NS.

The likelihood for a mass-only measurement is given by

$$\mathcal{L}_{\text{PSR-mass}}(\mathbf{E}) = \int_0^{M_{\text{TOV}}} dM \mathcal{P}(M|\text{PSR}), \quad (10)$$

where $\mathcal{P}(M|\text{PSR})$ is the posterior distribution of the pulsar’s mass and M_{TOV} is the maximum mass supported by the EOS with parameters \mathbf{E} . The posterior distributions of pulsar masses are typically well approximated by Gaussians²².

Recent X-ray observations of millisecond pulsars by NASA’s Neutron Star Interior Composition Explorer (NICER) mission have been used to simultaneously determine the mass and radius of these NSs^{65,96–99}. The corresponding likelihood is given by

$$\begin{aligned} \mathcal{L}_{\text{NICER}}(\mathbf{E}) &= \int dM \int dR \mathcal{P}_{\text{NICER}}(M, R) \frac{\pi(M, R|\mathbf{E})}{\pi(M, R|I)} \\ &\propto \int dM \int dR \mathcal{P}_{\text{NICER}}(M, R) \delta(R - R(M; \mathbf{E})) \\ &\propto \int dM \mathcal{P}_{\text{NICER}}(M, R = R(M; \mathbf{E})), \end{aligned} \quad (11)$$

where $\mathcal{P}_{\text{NICER}}(M, R)$ is the joint-posterior distribution of mass and radius as measured by NICER and we use the fact that (i) the radius is a function of mass for a given EOS, and (ii) that without further EOS information, e.g., through chiral EFT, the prior for the radius given mass is taken to be uniform.

Gravitational-wave inference

GW models

A complex frequency-domain GW signal is given by

$$h(f) = A(f)e^{-i\psi(f)}, \quad (12)$$

with the amplitude $A(f)$ and the GW phase $\psi(f)$. Because of the NS's finite size and internal structure, BNS and BHNS waveform models have to incorporate tidal contributions for an accurate interpretation of the binary coalescence. Such tidal contributions account for the deformation of the stars in their companions' external gravitational field^{100,101} and, once measured, allow to place constraints on the EOS governing the NS interior¹⁰²⁻¹⁰⁵. They are attractive because they convert energy from the orbital motion to a deformation of the stars, and lead to an accelerated inspiral. In the case of non-spinning compact objects, the leading-order tidal contribution depends on the tidal deformability

$$\tilde{\Lambda} = \frac{16}{13} \frac{(m_1 + 12m_2)m_1^4\Lambda_1 + (m_2 + 12m_1)m_2^4\Lambda_2}{(m_1 + m_2)^5} \quad (13)$$

with the individual tidal deformabilities $\Lambda_{1,2} = \frac{2}{3}k_2^{1,2}/C_{1,2}^5$ and the individual masses $m_{1,2}$. Here, $k_2^{1,2}$ are the Love numbers describing the static quadrupole deformation of one body inside the gravitoelectric field of the companion and $C_{1,2}$ are the individual compactnesses $C_{1,2} = m_{1,2}/R_{1,2}$ in isolation.

To date, there are three different types of BNS or BHNS models for the inspiral GW signal that are commonly used: Post-Newtonian (PN) models¹⁰⁶⁻¹⁰⁹, effective-one-body (EOB) models¹¹⁰⁻¹¹⁸, and phenomenological approximants¹¹⁹⁻¹²³. In the NMMA framework, we make use of the LALSuite¹²⁴ software package, in particular LAL-Simulation, so that the BNS and BHNS models used by the LIGO-Virgo-Kagra Collaborations can be easily employed. This includes:

- PN models such as `TaylorT2`, `TaylorT4`, or `TaylorF2` where a PN descriptions for the point-particle BBH baseline as well as the tidal description is employed,
- the most commonly used tidal EOB models `SEOBNRv4T`^{113,118,125}, its frequency-domain surrogate model¹²⁶, as well as the `TEOBResumS` model^{114,127} including its post-adiabatic accelerated version¹²⁸ which enables it being used during parameter estimation,
- and phenomenological models such as `IMRPhenomD_NRTidal`, `SEOBNRv4_ROM_NRTidal`, `IMRPhenomPv2_NRTidal`, `IMRPhenomD_NRTidalv2`, `SEOBNRv4_ROM_NRTidalv2`, `IMRPhenomPv2_NRTidalv2`¹²⁰⁻¹²², `PhenomNSBH`, and `SEOBNRv4_ROM_NRTidalv2_NSBH`^{123,129}.

GW analysis

By assuming stationary Gaussian noise, the GW likelihood $\mathcal{L}_{\text{GW}}(\boldsymbol{\theta})$ that the data d is a sum of noise and a GW signal h with parameters $\boldsymbol{\theta}$ is given by¹³⁰

$$\mathcal{L}_{\text{GW}} \propto \exp\left(-\frac{1}{2}\langle d - h(\boldsymbol{\theta}) | d - h(\boldsymbol{\theta}) \rangle\right), \quad (14)$$

where the inner product $\langle a | b \rangle$ is defined as

$$\langle a | b \rangle = 4\Re \int_{f_{\text{low}}}^{f_{\text{high}}} \frac{\tilde{a}(f)\tilde{b}^*(f)}{S_n(f)} df. \quad (15)$$

Here, $\tilde{a}(f)$ is the Fourier transform of $a(t)$, $*$ denotes complex conjugation, and $S_n(f)$ is the one-sided power spectral density of the noise. The choice of f_{low} and f_{high} depends on the type of binary that we are interested in. In our study, we will set f_{low} and f_{high} to 20 Hz and 2048 Hz, respectively. This is sufficient for capturing the inspiral up to the moment of merger for a typical BNS system in the advanced GW detector era.

Electromagnetic Signals

Kilonova models

Kilonova models are extracted using the 3D Monte Carlo radiative transfer code POSSIS¹³¹. The code can handle arbitrary geometries for the ejected material and produces spectra, lightcurves and polarization as a function of the observer viewing angle. Given an input model with defined densities ρ and compositions (i.e., electron fraction Y_e), the code generates Monte Carlo photon packets with initial location and energy sampled from the energy distribution from radioactive decay of r-process nuclei within the model. The latter depends on the mass/density distribution of the model and the assumed nuclear heating rates and thermalization efficiencies. The frequency of each Monte Carlo photon packet is sampled according to the temperature T in the ejecta, which is calculated at each time-step^{132,133}. Photon packets are then followed as they diffuse out of the ejected material and interact with matter via either electron scattering or bound-bound line transitions. Time- and wavelength-dependent opacities $\kappa_\lambda(\rho, T, Y_e, t)$ from Tanaka et al.¹³⁴ are implemented in the code and depend on the local properties of the ejecta (ρ , T , and Y_e). Spectral time series are extracted using the technique described by Bulla et al.¹³⁵ and used to construct broad-band lightcurves in any desired filter.

Supernova models

Templates available within the `SNCosmo` library¹³⁶ are used to model supernova spectra. Currently, the `salt2` model for Type Ia supernovae and the `nugent-hyper` model for hypernovae associated with long GRBs are implemented in the framework and have been used in the past³⁶. However, the framework is flexible enough such that additional templates for different types of supernovae can be added with minimal effort.

Kilonova/Supernova Inference

Our EM inference of kilonovae and GRB afterglows is based on the AB magnitude for a specific filter j , $m_i^j(t_i)$. We assume these measurements to be given as a time series at times t_i with a corresponding statistical error $\sigma_i^j \equiv \sigma^j(t_i)$. The likelihood function $\mathcal{L}_{\text{EM}}(\boldsymbol{\theta})$ then reads¹³⁷:

$$\mathcal{L}_{\text{EM}} \propto \exp\left(-\frac{1}{2} \sum_{ij} \frac{(m_i^j - m_i^{j,\text{est}}(\boldsymbol{\theta}))^2}{(\sigma_i^j)^2 + \sigma_{\text{sys}}^2}\right), \quad (16)$$

where $m_i^{j,\text{est}}(\boldsymbol{\theta})$ is the estimated AB magnitude for the parameters $\boldsymbol{\theta}$ and σ_{sys} is the additional error budget for accounting the systematic uncertainty within the electromagnetic signal modeling. The inclusion of σ_{sys} is equivalent to adding a shift of Δm to the light curve, for which marginalized with respect to a zero-mean normal distribution with a variance of σ_{sys}^2 .

This likelihood is equivalent to approximating the probability distribution of the spectral flux density f_ν to be a Log-normal distribution. The Log-normal distribution is a 2-parameter maximum entropy distribution with its support equals to the possible range for $f_\nu \in (0, \infty)$. There are two advantages of approximating f_ν with a Log-normal distribution: (i) if the uncertainty is larger or comparable to the measured value, it avoids having non-zero support for the nonphysical $f_\nu < 0$; (ii) if the uncertainty is much smaller than the measured value, the Log-normal distribution approaches the normal distribution.

For kilonovae, we use the same model presented in Dietrich et al.²². The model is controlled by four parameters, namely, the dynamical ejecta mass $m_{\text{dym}}^{\text{ej}}$, the disk wind ejecta mass $m_{\text{wind}}^{\text{ej}}$, the half-opening angle of the lanthanide-rich component Φ , and the

viewing angle θ_{obs} . Both the dynamical ejecta and the disk wind ejecta are described in methods section 4.

GRB Afterglows

In our framework, the computation of the GRB afterglow lightcurves is until now based on the publicly available semi-analytic code `afterglowpy`^{59,60}. The inclusion of other afterglow models is currently ongoing.

The GRB afterglow emission is produced by relativistic electrons gyrating around the magnetic field lines. These electrons are accelerated by the Fermi first-order acceleration (diffusive shock acceleration) and the magnetic field is assumed to be of turbulent nature, amplified by processes acting in collision-less shocks. The complex physics of electron acceleration at shocks is approximated by the equipartition parameters, ϵ_e and ϵ_B , denoting the fraction of the shock energy that goes into the relativistic electrons and magnetic field, respectively, and p , and the slope of the electron energy distribution $dn/d\gamma \propto \gamma^{-p}$, with n being the electron number density and γ being the electron Lorentz factor. The flux density of the curvature radiation is

$$F_\nu = \frac{1}{4\pi d_L^2} \int d\theta d\phi R^2 \sin(\theta) \frac{\epsilon_\nu}{\alpha_\nu} (1 - e^{-\tau}), \quad (17)$$

where τ is the optical depth and ϵ_ν and α_ν are the impassivity coefficient and absorption coefficient, respectively. For a fixed power-law distribution of electrons these can be approximated analytically¹³⁸. The synchrotron self-absorption is neglected in this work.

In order to capture the possible dependence of the GRB properties on the polar angle, the jet is discretized into a set of lateral axisymmetric (conical) layers, each of which is characterized by its initial velocity, mass, and angle. Several prescriptions for the initial angular distribution of the jet energy are available in the code. As default, we use the Gaussian jet model with $E \propto E_0 \exp(-\frac{1}{2}(\frac{\theta}{\theta_c})^2)$, where θ_c characterizes the width of the Gaussian. The jet truncation angle is θ_w . We assume the GRB jet to be powered by the accretion of mass from the disk onto the remnant black hole^{139–142}. Consequently, the jet energy is proportional to the leftover disk mass,

$$E_0 = \epsilon \times (1 - \xi) \times m_{\text{disk}}, \quad (18)$$

where ξ is the fraction of disk mass ejected as wind and ϵ is the fraction of residual disk mass converted into jet energy.

The dynamical evolution of these layers is computed semi-analytically using the "thin-shell approximation" casting energy-conservation equations and shock-jump conditions into a set of evolution equations for the blast wave velocity and radius. Within blast waves, the pressure gradient perpendicular to the normal leads to lateral expansion^{143,144}. In other words, the transverse pressure gradient adds the velocity along the tangent to the blast wave surface, forcing the latter to expand. The lateral expansion is important for late-time afterglow and is included in the code.

Finally, the flux density, F_ν , is obtained by equal arrival time surface integration, Eq. (17), taking into account relativistic effects, i.e., that the observed F_ν is composed of contributions from different blast waves that has emitted at different comoving time and at different frequencies.

Connecting Electromagnetic Signals to Source properties

To connect the observed GRB, kilonova, and GRB afterglow properties to the binary properties, we rely on phenomenological relations, i.e., fits based on numerical-relativity simulations. For our work, we use the

fits presented in Kruger et al.¹⁴⁵ and Dietrich et al.²² but emphasize that a variety of other fitting formulas exist in the literature^{20,53,57,146,147}.

In NMMA, the dynamical ejecta mass $m_{\text{dyn}}^{\text{ej}}$ is connected to the binary properties through the phenomenological relation¹⁴⁵

$$\frac{m_{\text{dyn,fit}}^{\text{ej}}}{10^{-3}M_\odot} = \left(\frac{a}{C_1} + b \left(\frac{m_2}{m_1} \right)^n + cC_1 \right) + (1 \leftrightarrow 2), \quad (19)$$

where m_i and C_i are the masses and the compactness of the two components of the binary with best-fit coefficients $a = -9.3335$, $b = 114.17$, $c = -337.56$, and $n = 1.5465$. This relation enables an accurate estimation of the ejecta mass with an error well-approximated by a zero-mean Gaussian with a standard deviation $0.004M_\odot$ ¹⁴⁵. Therefore, the dynamical ejecta mass can be approximated as

$$m_{\text{dyn}}^{\text{ej}} = m_{\text{dyn,fit}}^{\text{ej}} + \alpha, \quad (20)$$

where $\alpha \sim \mathcal{N}(\mu = 0, \sigma = 0.004M_\odot)$.

To determine the disk mass m_{disk} , we follow the description of Dietrich et al.²²,

$$\log_{10} \left(\frac{m_{\text{disk}}}{M_\odot} \right) = \quad (21)$$

$$\max \left(-3, a \left(1 + b \tanh \left(\frac{c - (m_1 + m_2)M_{\text{threshold}}^{-1}}{d} \right) \right) \right), \quad (22)$$

with a and b given by

$$a = a_o + \delta a \cdot \Delta, \quad b = b_o + \delta b \cdot \Delta, \quad (23)$$

where a_o , b_o , δa , δb , c , and d are free parameters. The parameter Δ is given by

$$\Delta = \frac{1}{2} \tanh(\beta(q - q_{\text{trans}})), \quad (24)$$

where $q \equiv m_2/m_1 \leq 1$ is the mass ratio and β and q_{trans} are free parameters. The best-fit model parameters are $a_o = -1.581$, $\delta a = -2.439$, $b_o = -0.538$, $\delta b = -0.406$, $c = 0.953$, $d = 0.0417$, $\beta = 3.910$, $q_{\text{trans}} = 0.900$. The threshold mass $M_{\text{threshold}}$ for a given EOS is estimated as¹⁴⁸

$$M_{\text{threshold}} = \left(2.38 - 3.606 \frac{M_{\text{TOV}}}{R_{1.6}} \right) M_{\text{TOV}}, \quad (25)$$

where M_{TOV} and $R_{1.6}$ are the maximum mass of a non-spinning NS and the radius of a $1.6M_\odot$ NS. We note that we assume that the disk-wind ejecta component is proportional to the disk mass, i.e., $m_{\text{wind}}^{\text{ej}} = \xi \times m_{\text{disk}}$.

Bayesian statistics

Based on Bayes' theorem, the posterior distribution of the parameters $p(\boldsymbol{\theta}|d, \mathcal{H})$ under hypothesis \mathcal{H} with data d is given by

$$p(\boldsymbol{\theta}|d, \mathcal{H}) = \frac{p(d|\boldsymbol{\theta}, \mathcal{H})p(\boldsymbol{\theta}|\mathcal{H})}{p(d|\mathcal{H})} \equiv \frac{\mathcal{L}(\boldsymbol{\theta})\pi(\boldsymbol{\theta})}{\mathcal{Z}(d)}, \quad (26)$$

where $\mathcal{L}(\boldsymbol{\theta})$, $\pi(\boldsymbol{\theta})$, and $\mathcal{Z}(d)$ are the likelihood, prior, and evidence, respectively. The prior describes our knowledge of the source or model parameters prior to the experiment or observation. The likelihood and evidence quantify how well the hypothesis describes the data for a given set of parameters and over the whole parameter space, respectively. Throughout our NMMA pipeline, all data analyses use Bayes' theorem but differences appear due to the functional form of the likelihood and its specific dependence on the source parameters. For example, the GW likelihood is evaluated with a cross-correlation between the data and the GW waveform and the EM signal analysis employs a

χ^2 log-likelihood between the predicted lightcurves with the observed apparent magnitude data, however, from a Bayesian viewpoint their treatment is equivalent only with different likelihood functions.

In addition to the posterior estimation, the evidence \mathcal{Z} carries additional information on the plausibility of a given hypothesis \mathcal{H} . The evidence is given by

$$\mathcal{Z}(d|\mathcal{H}) = \int d\theta p(d|\theta, \mathcal{H})p(\theta|\mathcal{H}) = \int d\theta \mathcal{L}(\theta)\pi(\theta), \quad (27)$$

which is the normalization constant for the posterior distribution. Moreover, we can compare the plausibilities of two hypotheses, \mathcal{H}_1 and \mathcal{H}_2 , by using the odd ratio \mathcal{O}_2^1 , which is given by

$$\mathcal{O}_2^1 = \frac{\mathcal{Z}_1 p(\mathcal{H}_1)}{\mathcal{Z}_2 p(\mathcal{H}_2)} \equiv \mathcal{B}_2^1 \Pi_2^1, \quad (28)$$

where \mathcal{B}_2^1 and Π_2^1 are the Bayes factor and prior odds, respectively. If $\mathcal{O}_2^1 > 1$, \mathcal{H}_1 is more plausible than \mathcal{H}_2 , and vice versa.

5 Data Availability

The datasets generated during the current study are available in the Zenodo repository <https://doi.org/10.5281/zenodo.6551053>. The GW data strain that we have analysed in this work was obtained from the Gravitational Wave Open Science Center (ref.¹⁴⁹ at <https://www.gw-openscience.org>), and the NICER data were obtained from Zenodo (<https://doi.org/10.5281/zenodo.3473466>, <https://doi.org/10.5281/zenodo.4670689> and <https://doi.org/10.5281/zenodo.4697625>).

6 Code Availability

The source code of the NMMA framework, which was used for this study, is publicly available at <https://github.com/nuclear-multimessenger-astronomy/nmma>. In addition, all employed GW models are available on <https://git.ligo.org/lscsoft>. The bilby and parallel bilby software packages are available at <https://git.ligo.org/lscsoft/bilby> and https://git.ligo.org/lscsoft/parallel_bilby, respectively.

References

1. Abbott, B. P. *et al.* GW170817: Observation of Gravitational Waves from a Binary Neutron Star Inspiral. *Phys. Rev. Lett.* **119**, 161101 (2017). 1710.05832.
2. Andreoni, I. *et al.* Follow up of GW170817 and its electromagnetic counterpart by Australian-led observing programs. *Publ. Astron. Soc. Austral.* **34**, e069 (2017). 1710.05846.
3. Chornock, R. *et al.* The Electromagnetic Counterpart of the Binary Neutron Star Merger LIGO/VIRGO GW170817. IV. Detection of Near-infrared Signatures of r-process Nucleosynthesis with Gemini-South. *Astrophys. J. Lett.* **848**, L19 (2017). 1710.05454.
4. Coulter, D. A. *et al.* Swope Supernova Survey 2017a (SSS17a), the Optical Counterpart to a Gravitational Wave Source. *Science* (2017). [Science358,1556(2017)], 1710.05452.
5. Evans, P. *et al.* Swift and NuSTAR observations of GW170817: detection of a blue kilonova. *Science* **358**, 1565 (2017). 1710.05437.
6. Kasliwal, M. M. *et al.* Spitzer mid-infrared detections of neutron star merger GW170817 suggests synthesis of the heaviest elements. *Monthly Notices of the Royal Astronomical Society* **510**, L7–L12 (2022). 1812.08708.
7. Kilpatrick, C. D. *et al.* Electromagnetic Evidence that SSS17a is the Result of a Binary Neutron Star Merger. *Science* **358**, 1583–1587 (2017). 1710.05434.
8. Lipunov, V. M. *et al.* MASTER Optical Detection of the First LIGO/Virgo Neutron Star Binary Merger GW170817. *Astrophys. J. Lett.* **850**, L1 (2017). 1710.05461.
9. McCully, C. *et al.* The Rapid Reddening and Featureless Optical Spectra of the optical counterpart of GW170817, AT 2017gfo, During the First Four Days. *Astrophys. J. Lett.* **848**, L32 (2017). 1710.05853.
10. Shappee, B. J. *et al.* Early Spectra of the Gravitational Wave Source GW170817: Evolution of a Neutron Star Merger. *Science* **358**, 1574 (2017). 1710.05432.
11. Tanvir, N. R. *et al.* The Emergence of a Lanthanide-Rich Kilonova Following the Merger of Two Neutron Stars. *Astrophys. J.* **848**, L27 (2017). 1710.05455.
12. Utsumi, Y. *et al.* J-GEM observations of an electromagnetic counterpart to the neutron star merger GW170817. *Publ. Astron. Soc. Jap.* **69**, 101 (2017). 1710.05848.
13. Margutti, R. *et al.* The Electromagnetic Counterpart of the Binary Neutron Star Merger LIGO/VIRGO GW170817. V. Rising X-ray Emission from an Off-Axis Jet. *Astrophys. J. Lett.* **848**, L20 (2017). 1710.05431.
14. Fong, W. *et al.* The Optical Afterglow of GW170817: An Off-axis Structured Jet and Deep Constraints on a Globular Cluster Origin. *Astrophys. J. Lett.* **883**, L1 (2019). 1908.08046.
15. Lamb, G. P. *et al.* The Optical Afterglow of GW170817 at One Year Post-merger. *Astrophys. J. Lett.* **870**, L15 (2019). 1811.11491.
16. Bauswein, A., Just, O., Janka, H.-T. & Stergioulas, N. Neutron-star radius constraints from GW170817 and future detections. *Astrophys. J.* **850**, L34 (2017). 1710.06843.
17. Ruiz, M., Shapiro, S. L. & Tsokaros, A. GW170817, General Relativistic Magnetohydrodynamic Simulations, and the Neutron Star Maximum Mass. *Phys. Rev.* **D97**, 021501 (2018). 1711.00473.
18. Radice, D., Perego, A., Zappa, F. & Bernuzzi, S. GW170817: Joint Constraint on the Neutron Star Equation of State from Multimessenger Observations. *Astrophys. J.* **852**, L29 (2018). 1711.03647.
19. Most, E. R., Weih, L. R., Rezzolla, L. & Schaffner-Bielich, J. New constraints on radii and tidal deformabilities of neutron stars from GW170817. *Phys. Rev. Lett.* **120**, 261103 (2018). 1803.00549.
20. Coughlin, M. W., Dietrich, T., Margalit, B. & Metzger, B. D. Multimessenger Bayesian parameter inference of a binary neutron star merger. *Monthly Notices of the Royal Astronomical Society: Letters* **489**, L91–L96 (2019). 1812.04803.
21. Capano, C. D. *et al.* Stringent constraints on neutron-star radii from multimessenger observations and nuclear theory. *Nature Astronomy* (2019). 1908.10352.
22. Dietrich, T. *et al.* Multimessenger constraints on the neutron-star equation of state and the Hubble constant. *Science* **370**, 1450–1453 (2020). 2002.11355.
23. Huth, S. *et al.* Constraining Neutron-Star Matter with Microscopic and Macroscopic Collisions. *arXiv:2107.06229* (2021).
24. Abbott, B. P. *et al.* A gravitational-wave standard siren measurement of the Hubble constant. *Nature*, 10.1038/nature24471 (2017). 1710.05835.
25. Guidorzi, C. *et al.* Improved Constraints on H_0 from a Combined Analysis of Gravitational-wave and Electromagnetic Emission from GW170817. *Astrophys. J.* **851**, L36 (2017). 1710.06426.
26. Hotokezaka, K. *et al.* A Hubble constant measurement from superluminal motion of the jet in GW170817. *Nature Astron.* (2019). 1806.10596.
27. Coughlin, M. W. *et al.* On standardizing kilonovae and their use as standard candles to measure the Hubble constant. *Phys. Rev. Research.* **2**, 022006 (2020). 1908.00889.
28. Wang, H. & Giannios, D. Multimessenger parameter estimation of GW170817: from jet structure to the Hubble constant. *Astrophys. J.* **908**, 200 (2021). 2009.04427.
29. Abbott, B. *et al.* Multi-messenger Observations of a Binary Neutron Star Merger. *Astrophys. J. Lett.* **848**, L12 (2017). 1710.05833.
30. Breschi, M. *et al.* AT2017gfo: Bayesian inference and model selection of multicomponent kilonovae and constraints on the neutron star equation of state. *Mon. Not. Roy. Astron. Soc.* **505**, 1661–1677 (2021). 2101.01201.
31. Nicholl, M. *et al.* Tight multimessenger constraints on the neutron star equation of state from GW170817 and a forward model for kilonova light-curve synthesis. *Mon. Not. Roy. Astron. Soc.* **505**, 3016–3032 (2021). 2102.02229.
32. Raaijmakers, G. *et al.* The Challenges Ahead for Multimessenger Analyses of Gravitational Waves and Kilonova: A Case Study on GW190425. *Astrophys. J.* **922**, 269 (2021). 2102.11569.
33. Pang, P. T. H. *et al.* Nuclear Physics Multimessenger Astrophysics Constraints on the Neutron Star Equation of State: Adding NICER’s PSR J0740+6620 Measurement. *Astrophys. J.* **922**, 14 (2021). 2105.08688.
34. Tews, I. *et al.* On the Nature of GW190814 and Its Impact on the Understanding of Supranuclear Matter. *Astrophys. J. Lett.* **908**, L1 (2021). 2007.06057.

35. Andreoni, I. *et al.* Fast-transient Searches in Real Time with ZTFReST: Identification of Three Optically Discovered Gamma-Ray Burst Afterglows and New Constraints on the Kilonova Rate. *Astrophys. J.* **918**, 63 (2021). 2104.06352.
36. Ahumada, T. *et al.* Discovery and confirmation of the shortest gamma-ray burst from a collapsar. *Nature Astron.* **5**, 917–927 (2021). 2105.05067.
37. Tews, I., Carlson, J., Gandolfi, S. & Reddy, S. Constraining the speed of sound inside neutron stars with chiral effective field theory interactions and observations. *Astrophys. J.* **860**, 149 (2018). 1801.01923.
38. Tews, I., Margueron, J. & Reddy, S. Critical examination of constraints on the equation of state of dense matter obtained from GW170817. *Phys. Rev. C* **98**, 045804 (2018). 1804.02783.
39. Lynn, J. E. *et al.* Chiral Three-Nucleon Interactions in Light Nuclei, Neutron- α Scattering, and Neutron Matter. *Phys. Rev. Lett.* **116**, 062501 (2016). 1509.03470.
40. Holt, J. W. & Kaiser, N. Equation of state of nuclear and neutron matter at third-order in perturbation theory from chiral effective field theory. *Phys. Rev. C* **95**, 034326 (2017). 1612.04309.
41. Drischler, C., Hebeler, K. & Schwenk, A. Chiral interactions up to next-to-next-to-next-to-leading order and nuclear saturation. *Phys. Rev. Lett.* **122**, 042501 (2019). 1710.08220.
42. Piarulli, M., Bombaci, I., Logoteta, D., Lovato, A. & Wiringa, R. B. Benchmark calculations of pure neutron matter with realistic nucleon-nucleon interactions. *Phys. Rev. C* **101**, 045801 (2020). 1908.04426.
43. Keller, J., Wellenhofer, C., Hebeler, K. & Schwenk, A. Neutron matter at finite temperature based on chiral effective field theory interactions. *Phys. Rev. C* **103**, 055806 (2021). 2011.05855.
44. Russotto, P. *et al.* Results of the ASY-EOS experiment at GSI: The symmetry energy at suprasaturation density. *Phys. Rev. C* **94**, 034608 (2016). 1608.04332.
45. Adhikari, D. *et al.* Accurate Determination of the Neutron Skin Thickness of ^{208}Pb through Parity-Violation in Electron Scattering. *Phys. Rev. Lett.* **126**, 172502 (2021). 2102.10767.
46. Antoniadis, J. *et al.* A Massive Pulsar in a Compact Relativistic Binary. *Science* **340**, 6131 (2013). 1304.6875.
47. Arzoumanian, Z. *et al.* The NANOGrav 11-year Data Set: High-precision timing of 45 Millisecond Pulsars. *Astrophys. J. Suppl.* **235**, 37 (2018). 1801.01837.
48. Cromartie, H. T. *et al.* Relativistic Shapiro delay measurements of an extremely massive millisecond pulsar. *Nature Astron.* **4**, 72–76 (2019). 1904.06759.
49. Kurkela, A., Fraga, E. S., Schaffner-Bielich, J. & Vuorinen, A. Constraining neutron star matter with Quantum Chromodynamics. *Astrophys. J.* **789**, 127 (2014). 1402.6618.
50. Komoltsev, O. & Kurkela, A. How perturbative QCD constrains the Equation of State at Neutron-Star densities. *arXiv:2111.05350* (2021).
51. Vallisneri, M. Use and abuse of the Fisher information matrix in the assessment of gravitational-wave parameter-estimation prospects. *Phys. Rev. D* **77**, 042001 (2008). gr-qc/0703086.
52. Abbott, B. P. *et al.* Properties of the binary neutron star merger GW170817. *Phys. Rev. X* **9**, 011001 (2019). 1805.11579.
53. Coughlin, M. W. *et al.* Constraints on the neutron star equation of state from $\text{a}2017\text{gfo}$ using radiative transfer simulations. *Monthly Notices of the Royal Astronomical Society* **480**, 3871–3878 (2018). 1805.09371.
54. Heinzl, J. *et al.* Comparing inclination dependent analyses of kilonova transients. *Mon. Not. Roy. Astron. Soc.* **502**, 3057–3065 (2021). 2010.10746.
55. Bulla, M. The critical role of nuclear heating rates, thermalization efficiencies and opacities for kilonova modelling and parameter inference (2022). 2211.14348.
56. Siegel, D. M. GW170817—the first observed neutron star merger and its kilonova: implications for the astrophysical site of the r-process. *Eur. Phys. J. A* **55**, 203 (2019). 1901.09044.
57. Radice, D. *et al.* Binary Neutron Star Mergers: Mass Ejection, Electromagnetic Counterparts and Nucleosynthesis. *Astrophys. J.* **869**, 130 (2018). 1809.11161.
58. Troja, E. *et al.* A year in the life of GW 170817: the rise and fall of a structured jet from a binary neutron star merger. *Mon. Not. Roy. Astron. Soc.* **489**, 1919–1926 (2019). 1808.06617.
59. van Eerten, H., Zhang, W. & MacFadyen, A. Off-Axis Gamma-Ray Burst Afterglow Modeling Based On A Two-Dimensional Axisymmetric Hydrodynamics Simulation. *Astrophys. J.* **722**, 235–247 (2010). 1006.5125.
60. Ryan, G., van Eerten, H., Piro, L. & Troja, E. Gamma-Ray Burst Afterglows in the Multimessenger Era: Numerical Models and Closure Relations. *Astrophys. J.* **896**, 166 (2020). 1909.11691.
61. Shrestha, M. *et al.* Impact of jets on kilonova photometric and polarimetric emission from binary neutron star mergers. *Mon. Not. Roy. Astron. Soc.* **523**, 2990–3000 (2023). 2303.14277.
62. Anand, S. *et al.* Chemical Distribution of the Dynamical Ejecta in the Neutron Star Merger GW170817 (2023). 2307.11080.
63. Essick, R., Tews, I., Landry, P., Reddy, S. & Holz, D. E. Direct Astrophysical Tests of Chiral Effective Field Theory at Supranuclear Densities. *Phys. Rev. C* **102**, 055803 (2020). 2004.07744.
64. Raaijmakers, G. *et al.* Constraints on the Dense Matter Equation of State and Neutron Star Properties from NICER’s Mass–Radius Estimate of PSR J0740+6620 and Multimessenger Observations. *Astrophys. J. Lett.* **918**, L29 (2021). 2105.06981.
65. Miller, M. C. *et al.* The Radius of PSR J0740+6620 from NICER and XMM-Newton Data. *Astrophys. J. Lett.* **918**, L28 (2021). 2105.06979.
66. Baym, G., Pethick, C. & Sutherland, P. The Ground State of Matter at High Densities: Equation of State and Stellar Models. *Astrophys. J.* **170**, 299+ (1971).
67. Chamel, N. & Haensel, P. Physics of Neutron Star Crusts. *Living Rev. Rel.* **11**, 10 (2008). 0812.3955.
68. Tews, I. *et al.* Nuclear Forces for Precision Nuclear Physics – a collection of perspectives. *arXiv* (2022). 2202.01105.
69. Krüger, T., Tews, I., Hebeler, K. & Schwenk, A. Neutron matter from chiral effective field theory interactions. *Phys. Rev. C* **88**, 025802 (2013). 1304.2212.
70. Epelbaum, E., Hammer, H.-W. & Meissner, U.-G. Modern Theory of Nuclear Forces. *Rev. Mod. Phys.* **81**, 1773–1825 (2009). 0811.1338.
71. Machleidt, R. & Entem, D. R. Chiral effective field theory and nuclear forces. *Phys. Rept.* **503**, 1–75 (2011). 1105.2919.
72. Drischler, C., Melendez, J. A., Furnstahl, R. J. & Phillips, D. R. Quantifying uncertainties and correlations in the nuclear-matter equation of state. *Phys. Rev. C* **102**, 054315 (2020). 2004.07805.
73. Weinberg, S. Nuclear forces from chiral Lagrangians. *Phys. Lett. B* **251**, 288–292 (1990).
74. Weinberg, S. Effective chiral Lagrangians for nucleon - pion interactions and nuclear forces. *Nucl. Phys. B* **363**, 3–18 (1991).
75. Weinberg, S. Three body interactions among nucleons and pions. *Phys. Lett. B* **295**, 114–121 (1992). hep-ph/9209257.
76. Epelbaum, E., Krebs, H. & Meißner, U.-G. Improved chiral nucleon-nucleon potential up to next-to-next-to-next-to-leading order. *Eur. Phys. J. A* **51**, 53 (2015). URL <http://dx.doi.org/10.1140/epja/i2015-15053-8>. 1412.0142.
77. Drischler, C., Furnstahl, R. J., Melendez, J. A. & Phillips, D. R. How Well Do We Know the Neutron-Matter Equation of State at the Densities Inside Neutron Stars? A Bayesian Approach with Correlated Uncertainties. *Phys. Rev. Lett.* **125**, 202702 (2020). 2004.07232.
78. Ekström, A., Hagen, G., Morris, T. D., Papenbrock, T. & Schwartz, P. D. Δ isobars and nuclear saturation. *Phys. Rev. C* **97**, 024332 (2018). 1707.09028.
79. Tews, I., Krüger, T., Hebeler, K. & Schwenk, A. Neutron matter at next-to-next-to-next-to-leading order in chiral effective field theory. *Phys. Rev. Lett.* **110**, 032504 (2013). 1206.0025.
80. Carbone, A., Cipollone, A., Barbieri, C., Rios, A. & Polls, A. Self-consistent Green’s functions formalism with three-body interactions. *Phys. Rev. C* **88**, 054326 (2013). 1310.3688.
81. Hagen, G. *et al.* Coupled-cluster calculations of nucleonic matter. *Phys. Rev. C* **89**, 014319 (2014). 1311.2925.
82. Carlson, J. *et al.* Quantum Monte Carlo methods for nuclear physics. *Rev. Mod. Phys.* **87**, 1067 (2015).
83. Schmidt, K. E. & Fantoni, S. A quantum Monte Carlo method for nucleon systems. *Phys. Lett. B* **446**, 99–103 (1999).
84. Tews, I. Spectrum of shear modes in the neutron-star crust: Estimating the nuclear-physics uncertainties. *Phys. Rev. C* **95**, 015803 (2017). 1607.06998.
85. Read, J. S., Lackey, B. D., Owen, B. J. & Friedman, J. L. Constraints on a phenomenologically parameterized neutron-star equation of state. *Phys. Rev. D* **79**, 124032 (2009). 0812.2163.
86. Hebeler, K., Lattimer, J., Pethick, C. & Schwenk, A. Equation of state and neutron star properties constrained by nuclear physics and observation. *Astrophys. J.* **773**, 11 (2013). 1303.4662.
87. Annala, E., Gorda, T., Kurkela, A. & Vuorinen, A. Gravitational-wave constraints on the neutron-star-matter Equation of State. *Phys. Rev. Lett.* **120**, 172703 (2018). 1711.02644.
88. Tews, I., Margueron, J. & Reddy, S. Critical examination of constraints on the equation of state of dense matter obtained from GW170817. *Phys. Rev. C* **98**, 045804 (2018). 1804.02783.
89. Greif, S., Raaijmakers, G., Hebeler, K., Schwenk, A. & Watts, A. Equation of state sensitivities when inferring neutron star and dense matter properties. *Mon. Not. Roy. Astron. Soc.* **485**, 5363–5376 (2019). 1812.08188.

90. Essick, R., Landry, P. & Holz, D. E. Nonparametric Inference of Neutron Star Composition, Equation of State, and Maximum Mass with GW170817. *Phys. Rev. D* **101**, 063007 (2020). 1910.09740.
91. McLerran, L. & Reddy, S. Quarkyonic Matter and Neutron Stars. *Phys. Rev. Lett.* **122**, 122701 (2019). 1811.12503.
92. Jeong, K. S., McLerran, L. & Sen, S. Dynamically generated momentum space shell structure of quarkyonic matter via an excluded volume model. *Phys. Rev. C* **101**, 035201 (2020). 1908.04799.
93. Sen, S. & Sivertsen, L. Mass and Radius Relations of Quarkyonic Stars Using an Excluded-volume Model. *Astrophys. J.* **915**, 109 (2021). 2011.04681.
94. Margueron, J., Hansen, H., Proust, P. & Chanfray, G. Quarkyonic stars with isospin-flavor asymmetry. *Phys. Rev. C* **104**, 055803 (2021). 2103.10209.
95. Gandolfi, S., Carlson, J. & Reddy, S. The maximum mass and radius of neutron stars and the nuclear symmetry energy. *Phys. Rev. C* **85**, 032801 (2012). 1101.1921.
96. Wolff, M. T. *et al.* NICER Detection of Thermal X-Ray Pulsations from the Massive Millisecond Pulsars PSR J0740+6620 and PSR J1614–2230. *Astrophys. J. Lett.* **918**, L26 (2021). 2105.06978.
97. Miller, M. C. *et al.* PSR J0030+0451 Mass and Radius from NICER Data and Implications for the Properties of Neutron Star Matter. *Astrophys. J. Lett.* **887**, L24 (2019). 1912.05705.
98. Riley, T. E. *et al.* A NICER View of PSR J0030+0451: Millisecond Pulsar Parameter Estimation. *Astrophys. J. Lett.* **887**, L21 (2019). 1912.05702.
99. Riley, T. E. *et al.* A NICER View of the Massive Pulsar PSR J0740+6620 Informed by Radio Timing and XMM-Newton Spectroscopy. *Astrophys. J. Lett.* **918**, L27 (2021). 2105.06980.
100. Damour, T. & Nagar, A. Relativistic tidal properties of neutron stars. *Phys. Rev. D* **80**, 084035 (2009). 0906.0096.
101. Hinderer, T., Lackey, B. D., Lang, R. N. & Read, J. S. Tidal deformability of neutron stars with realistic equations of state and their gravitational wave signatures in binary inspiral. *Phys. Rev. D* **81**, 123016 (2010). 0911.3535.
102. Abbott, B. P. *et al.* Multi-messenger Observations of a Binary Neutron Star Merger. *Astrophys. J. Lett.* **848**, L12 (2017). 1710.05833.
103. Abbott, B. P. *et al.* GW170817: Measurements of neutron star radii and equation of state. *Phys. Rev. Lett.* **121**, 161101 (2018). 1805.11581.
104. Abbott, B. P. *et al.* Model comparison from LIGO–Virgo data on GW170817’s binary components and consequences for the merger remnant. *Class. Quant. Grav.* **37**, 045006 (2020). 1908.01012.
105. Carney, M. F., Wade, L. E. & Irwin, B. S. Comparing two models for measuring the neutron star equation of state from gravitational-wave signals. *Phys. Rev. D* **98**, 063004 (2018). 1805.11217.
106. Damour, T., Nagar, A. & Villain, L. Measurability of the tidal polarizability of neutron stars in late-inspiral gravitational-wave signals. *Phys. Rev. D* **85**, 123007 (2012). 1203.4352.
107. Abdelsalhin, T., Gualtieri, L. & Pani, P. Post-Newtonian spin-tidal couplings for compact binaries. *arXiv:1805.01487* (2018).
108. Landry, P. Rotational-tidal phasing of the binary neutron star waveform. *arXiv:1805.01882* (2018).
109. Jiménez Forteza, X., Abdelsalhin, T., Pani, P. & Gualtieri, L. Impact of high-order tidal terms on binary neutron-star waveforms. *Phys. Rev. D* **98**, 124014 (2018). 1807.08016.
110. Buonanno, A. & Damour, T. Effective one-body approach to general relativistic two-body dynamics. *Phys. Rev. D* **59**, 084006 (1999). gr-qc/9811091.
111. Damour, T. & Nagar, A. Effective One Body description of tidal effects in inspiralling compact binaries. *Phys. Rev. D* **81**, 084016 (2010). 0911.5041.
112. Hotokezaka, K., Kyutoku, K., Okawa, H. & Shibata, M. Exploring tidal effects of coalescing binary neutron stars in numerical relativity. II. Long-term simulations. *Phys. Rev. D* **91**, 064060 (2015). 1502.03457.
113. Hinderer, T. *et al.* Effects of neutron-star dynamic tides on gravitational waveforms within the effective-one-body approach. *Phys. Rev. Lett.* **116**, 181101 (2016). 1602.00599.
114. Akcay, S. *et al.* Effective-one-body multipolar waveform for tidally interacting binary neutron stars up to merger. *Phys. Rev. D* **99**, 044051 (2019). 1812.02744.
115. Bernuzzi, S., Nagar, A., Dietrich, T. & Damour, T. Modeling the Dynamics of Tidally Interacting Binary Neutron Stars up to the Merger. *Phys. Rev. Lett.* **114**, 161103 (2015). 1412.4553.
116. Dietrich, T. & Hinderer, T. Comprehensive comparison of numerical relativity and effective-one-body results to inform improvements in waveform models for binary neutron star systems. *Phys. Rev. D* **95**, 124006 (2017). 1702.02053.
117. Nagar, A. *et al.* Time-domain effective-one-body gravitational waveforms for coalescing compact binaries with nonprecessing spins, tides and self-spin effects. *Phys. Rev. D* **98**, 104052 (2018). 1806.01772.
118. Steinhoff, J., Hinderer, T., Dietrich, T. & Foucart, F. Spin effects on neutron star fundamental-mode dynamical tides: Phenomenology and comparison to numerical simulations. *Phys. Rev. Res.* **3**, 033129 (2021). 2103.06100.
119. Kawaguchi, K. *et al.* Frequency-domain gravitational waveform models for inspiraling binary neutron stars. *Phys. Rev. D* **97**, 044044 (2018). 1802.06518.
120. Dietrich, T., Bernuzzi, S. & Tichy, W. Closed-form tidal approximants for binary neutron star gravitational waveforms constructed from high-resolution numerical relativity simulations. *Phys. Rev. D* **96**, 121501 (2017). 1706.02969.
121. Dietrich, T. *et al.* Matter imprints in waveform models for neutron star binaries: Tidal and self-spin effects. *Phys. Rev. D* **99**, 024029 (2019). 1804.02235.
122. Dietrich, T. *et al.* Improving the NRTidal model for binary neutron star systems. *Phys. Rev. D* **100**, 044003 (2019). 1905.06011.
123. Thompson, J. E. *et al.* Modeling the gravitational wave signature of neutron star black hole coalescences. *Phys. Rev. D* **101**, 124059 (2020). 2002.08383.
124. LIGO Scientific Collaboration. LIGO Algorithm Library - LALSuite. free software (GPL) (2018).
125. Steinhoff, J., Hinderer, T., Buonanno, A. & Taracchini, A. Dynamical Tides in General Relativity: Effective Action and Effective-One-Body Hamiltonian. *Phys. Rev. D* **94**, 104028 (2016). 1608.01907.
126. Lackey, B. D., Pürrer, M., Taracchini, A. & Marsat, S. Surrogate model for an aligned-spin effective one body waveform model of binary neutron star inspirals using Gaussian process regression. *Phys. Rev. D* **100**, 024002 (2019). 1812.08643.
127. Nagar, A. *et al.* Nonlinear-in-spin effects in effective-one-body waveform models of spin-aligned, inspiralling, neutron star binaries. *Phys. Rev. D* **99**, 044007 (2019). 1812.07923.
128. Nagar, A. & Retegno, P. Efficient effective one body time-domain gravitational waveforms. *Phys. Rev. D* **99**, 021501 (2019). 1805.03891.
129. Matas, A. *et al.* Aligned-spin neutron-star–black-hole waveform model based on the effective-one-body approach and numerical-relativity simulations. *Phys. Rev. D* **102**, 043023 (2020). 2004.10001.
130. Veitch, J. *et al.* Parameter estimation for compact binaries with ground-based gravitational-wave observations using the LALInference software library. *Phys. Rev. D* **91**, 042003 (2015). 1409.7215.
131. Bulla, M. POSSIS: predicting spectra, light curves and polarization for multi-dimensional models of supernovae and kilonovae. *Mon. Not. Roy. Astron. Soc.* **489**, 5037–5045 (2019). 1906.04205.
132. Mazzali, P. A. & Lucy, L. B. The Application of Monte Carlo methods to the synthesis of early-time supernovae spectra. *Astron. Astrophys.* **279**, 447 (1993).
133. Magee, M. R., Sim, S. A., Kotak, R. & Kerzendorf, W. E. Modelling the early time behaviour of type Ia supernovae: effects of the ^{56}Ni distribution. *Astron. Astrophys.* **614**, A115 (2018). 1803.04436.
134. Tanaka, M., Kato, D., Gaigalas, G. & Kawaguchi, K. Systematic opacity calculations for kilonovae. *Monthly Notices of the Royal Astronomical Society* **496**, 1369–1392 (2020). 1906.08914.
135. Bulla, M., Sim, S. A. & Kromer, M. Polarization spectral synthesis for Type Ia supernova explosion models. *Monthly Notices of the Royal Astronomical Society* **450**, 967–981 (2015). 1503.07002.
136. Barbary, K. *et al.* Sncosmo (2022). URL <https://doi.org/10.5281/zenodo.6363879>. If you use Sncosmo, please cite it using these metadata.
137. Coughlin, M. *et al.* Toward Rapid Transient Identification and Characterization of Kilonovae. *Astrophys. J.* **849**, 12 (2017). 1708.07714.
138. Sari, R., Piran, T. & Narayan, R. Spectra and light curves of gamma-ray burst afterglows. *Astrophys. J. Lett.* **497**, L17 (1998). astro-ph/9712005.
139. Eichler, D., Livio, M., Piran, T. & Schramm, D. N. Nucleosynthesis, Neutrino Bursts and Gamma-Rays from Coalescing Neutron Stars. *Nature* **340**, 126–128 (1989).
140. Paczynski, B. Cosmological gamma-ray bursts. *Acta Astron.* **41**, 257–267 (1991).
141. Meszaros, P. & Rees, M. J. Tidal heating and mass loss in neutron star binaries - Implications for gamma-ray burst models. *Astrophys. J.* **397**, 570–575 (1992).
142. Narayan, R., Paczynski, B. & Piran, T. Gamma-ray bursts as the death throes of massive binary stars. *Astrophys. J.* **395**, L83–L86 (1992). astro-ph/9204001.

143. van Eerten, H., Leventis, K., Meliani, Z., Wijers, R. & Keppens, R. Gamma-ray burst afterglows from trans-relativistic blast wave simulations. *Mon. Not. Roy. Astron. Soc.* **403**, 300 (2010). 0909.2446.
144. Granot, J. & Piran, T. On the lateral expansion of gamma-ray burst jets. *Monthly Notices of the Royal Astronomical Society* **421**, 570–587 (2012). URL <https://doi.org/10.1111/j.1365-2966.2011.20335.x>. astro-ph/1109.6468.
145. Krüger, C. J. & Foucart, F. Estimates for Disk and Ejecta Masses Produced in Compact Binary Mergers. *Phys. Rev. D* **101**, 103002 (2020). 2002.07728.
146. Dietrich, T. & Ujevic, M. Modeling dynamical ejecta from binary neutron star mergers and implications for electromagnetic counterparts. *Class. Quant. Grav.* **34**, 105014 (2017). 1612.03665.
147. Nedora, V. *et al.* Mapping dynamical ejecta and disk masses from numerical relativity simulations of neutron star mergers. *Class. Quant. Grav.* **39**, 015008 (2022). 2011.11110.
148. Agathos, M. *et al.* Inferring Prompt Black-Hole Formation in Neutron Star Mergers from Gravitational-Wave Data. *Phys. Rev. D* **101**, 044006 (2020). 1908.05442.
149. Vallisneri, M., Kanner, J., Williams, R., Weinstein, A. & Stephens, B. The LIGO Open Science Center. *J. Phys. Conf. Ser.* **610**, 012021 (2015). 1410.4839.
150. Rasmussen, C. E. & Williams, C. K. I. *Gaussian Processes for Machine Learning* (MIT Press, 2006).
151. Pedregosa, F. *et al.* Scikit-learn: Machine learning in Python. *Journal of Machine Learning Research* **12**, 2825–2830 (2011).
152. Almualla, M. *et al.* Using Neural Networks to Perform Rapid High-Dimensional Kilonova Parameter Inference. *arXiv:2112.15470* (2021).
153. Abadi, M. *et al.* TensorFlow: Large-scale machine learning on heterogeneous systems (2015). URL <https://www.tensorflow.org/>. Software available from tensorflow.org.
154. Kasen, D., Metzger, B., Barnes, J., Quataert, E. & Ramirez-Ruiz, E. Origin of the heavy elements in binary neutron-star mergers from a gravitational wave event. *Nature*, *10.1038/nature24453* (2017). 1710.05463.
155. Kunert, N., Pang, P. T. H., Tews, I., Coughlin, M. W. & Dietrich, T. Quantifying modeling uncertainties when combining multiple gravitational-wave detections from binary neutron star sources. *Phys. Rev. D* **105**, L061301 (2022). 2110.11835.
156. Speagle, J. S. dynesty: a dynamic nested sampling package for estimating Bayesian posteriors and evidences. *Mon. Not. Roy. Astron. Soc.* **493**, 3132–3158 (2020). 1904.02180.
157. Smith, R. J. E., Ashton, G., Vajpeyi, A. & Talbot, C. Massively parallel Bayesian inference for transient gravitational-wave astronomy. *Mon. Not. Roy. Astron. Soc.* **498**, 4492–4502 (2020). 1909.11873.
158. Handley, W., Hobson, M. & Lasenby, A. PolyChord: nested sampling for cosmology. *Mon. Not. Roy. Astron. Soc.* **450**, L61–L65 (2015). 1502.01856.
159. Samajdar, A. & Dietrich, T. Waveform systematics for binary neutron star gravitational wave signals: effects of the point-particle baseline and tidal descriptions. *Phys. Rev.* **D98**, 124030 (2018). 1810.03936.
160. Samajdar, A. & Dietrich, T. Waveform systematics for binary neutron star gravitational wave signals: Effects of spin, precession, and the observation of electromagnetic counterparts. *Phys. Rev.* **D100**, 024046 (2019). 1905.03118.

7 Acknowledgements

We thank N. Andersson, R. Essick, P. Landry, and J. Margueron for insightful discussions. P.T.H.P and C.V.D.B. are supported by the research program of the Netherlands Organization for Scientific Research (NWO). T.D. acknowledges support of the Daimler and Benz Foundation. M.W.C. acknowledges support from the National Science Foundation with grant numbers PHY-2308862 and OAC-2117997. M.B. acknowledges support from the Swedish Research Council (Reg. no. 2020-03330). The work of I.T. was supported by the U.S. Department of Energy, Office of Science, Office of Nuclear Physics, under contract No. DE-AC52-06NA25396, by the Laboratory Directed Research and Development program of Los Alamos National Laboratory under project number 20220658ER, and by the U.S. Department of Energy, Office of Science, Office of Advanced Scientific Computing Research, Scientific Discovery through Advanced Computing (SciDAC) program. J.H. acknowledges support from the National Science Foundation with grant number PHY-1806990. Funded/Co-funded by the European Union (ERC, SMARt, 101076369). Views and opinions expressed are however those of the author(s) only and do not necessarily reflect those of the European Union or the European Research Council. Neither the European Union nor the granting authority can be held responsible for them.

Computations have been performed on the Minerva HPC cluster of the Max-Planck-Institute for Gravitational Physics and on SuperMUC-NG (LRZ) under project number pn56zo. Computational resources have also been provided by the Los Alamos National Laboratory Institutional Computing Program, which is supported by the U.S. Department of Energy National Nuclear Security Administration under Contract No. 89233218CNA000001, and by the National Energy Research Scientific Computing Center (NERSC), which is supported by the U.S. Department of Energy, Office of Science, under contract No. DE-AC02-05CH11231. Resources supporting this work were provided by the Minnesota Supercomputing Institute (MSI) at University of Minnesota under the project “Identification of Variable Objects in the Zwicky Transient Facility,” and the Supercomputing Laboratory at King Abdullah University of Science and Technology (KAUST) in Thuwal, Saudi Arabia. This research has made use of data, software and/or web tools obtained from the Gravitational Wave Open Science Center (<https://www.gw-openscience.org>), a service of LIGO Laboratory, the LIGO Scientific Collaboration and the Virgo Collaboration. This material is based upon work supported by NSF’s LIGO Laboratory which is a major facility fully funded by the National Science Foundation. Virgo is funded by the French Centre National de Recherche Scientifique (CNRS), the Italian Istituto Nazionale della Fisica Nucleare (INFN) and the Dutch Nikhef, with contributions by Polish and Hungarian institutes.

8 Author Contributions Statement

Conceptualisation: PTHP, TD, MC, MB, IT, CVDB;
Methodology: PTHP, TD, MC, MB, IT, MA, SA, CVDB;
Data curation: PTHP, MC, MA;
Software: PTHP, TD, MC, MB, IT, MA, TB, WK, NK, GM, BR, NS, AT, SA, RV, JH, PS, RSh, RSo, CVDB;
Validation: PTHP, MC;
Formal analysis: PTHP, MC;
Resources: TD, MC, MB, IT;
Funding acquisition: TD, MWC, MB, IT;
Project administration: PTHP, TD, MC, MB, IT, CVDB;
Supervision: PTHP, TD, MC, MB, IT;
Visualisation: PTHP, TD, MC, MB, IT, NK;
Writing—original draft: PTHP, TD, MC, MB, IT, NK, VN, PS;
Writing—review and editing: PTHP, TD, MC, MB, IT, NK, VN.

9 Competing Interests Statement

The authors declare no competing interests.

10 Correspondence

Prof. Dr. Tim Dietrich, tim.dietrich@uni-potsdam.de

Supplementary Material

Computing generic kilonova lightcurves.

Gaussian Process Regression: Because we are given vectors of photometry or spectra from radiative transfer simulations, we require methods to interpolate between these grids. If we denote the parameters of the models as Θ^j and the vectors of data as τ , parameterized by the i -th time index, we can create matrices of simulations as $\mathcal{T}_{ij} = [\tau_i(\Theta^j)]$. From these matrices, there are a variety of ways to interpolate these vectors, including direct interpolation of the vectors. Here, instead, we interpolate the principal components of each τ_i . To compute the principal components, we take the singular value decomposition (SVD) of this matrix

$$\mathcal{T} = V\Sigma U^\top. \quad (29)$$

The SVD computes orthonormal basis vectors in the columns and rows of V and U . With this new basis, we can project our original τ_i onto the left-singular vector basis

$$s_k(\Theta^j) = V_{ki}^\top \tau_i(\Theta^j), \quad (30)$$

where s_k are the weights of the principal components of the input data \mathcal{T}_{ij} . This method has the benefit of maximizing the variance in each subsequent basis vector, meaning we can truncate this sum to minimize computational resources; in our case, we find that using the first 10 basis vectors is sufficient for a reliable representation of the lightcurves.

To interpolate the principal component eigenvalues, we use Gaussian process regression (GPR)¹⁵⁰, which relies on the assumption that the correlation between neighboring values can be represented by a multivariate Gaussian distribution. The covariance between function values is known as a ‘kernel’ function, with many kernel functions commonly used in the literature; in our analysis, we use a rational-quadratic kernel function implemented in `sci-kit learn`¹⁵¹:

$$k(\Theta^i, \Theta^j) = \left(1 + \frac{d(\Theta^i, \Theta^j)^2}{2\alpha l^2}\right)^{-\alpha} \quad (31)$$

where $\alpha = 0.1$ and $l = 1.0$ for our implementation.

As is common in GPR-based interpolation, we first normalize the components of $s_k(\Theta^j)$ by subtracting the minimum value and dividing by the difference between the maximum and minimum value. After the interpolation, the de-whitened values are projected back into the time domain:

$$\tau_i(\Theta^j) = V_{ik} s_k(\Theta^j) \quad (32)$$

Finally, the interpolated $\tau_i(\Theta^j)$ is then used for the computation of the likelihood.

Neural Networks: Another alternative method for the grid interpolation is a feed-forward neural network (NN) which can predict the kilonova lightcurves based on the input parameters used by the chosen model¹⁵². The main advantage of this approach is it to reduce the memory footprint for the lightcurves computation.

To train the NN, we use about 2000 lightcurves computed with the full radiative transfer code POSSIS¹³¹. These lightcurves are split into a training data set of 90% and an evaluation dataset that contains 10% of all lightcurves. In the pre-processing stage, all the data was normalized between 0 and 1 via the usual MinMax normalization method, and similar to the GPR method, we used PCA data reduction to reduce the dimensions of the output parameter space to 10 components. In addition, we use simple linear interpolation for the cases in which the requested time interval is larger than the original in-hand data.

To develop our NN, we used Keras API from TENSORFLOW¹⁵³. Our NN comprises an input layer with the same number of neurons as the input parameter space, three dense hidden layers with 64, 128, and 128 neurons each, and an output layer with ten neurons for the bolometric luminosity and the nine observational bands. We use the Adam optimizer with a learning rate of 0.01 and a Rectified linear unit as activation function. Finally, the NN is trained using a batch size of 32, epoch count of 15, and mean squared error (MSE) as loss function. To reconstruct the real lightcurves, a series of inverse transformations is applied with respect to the PCA and the normalization. Overall a MSE of 0.0022 is achieved.

EOS Sampling. For a set of EOSs, such as our sets constrained by chiral EFT, our framework is able to directly sample over EOSs instead of sampling over the masses and tidal deformabilities independently. Since these EOSs relate masses and tidal deformabilities based on nuclear-physics information, the tidal deformabilities can be computed for a given mass and EOS according to

$$p(\Lambda_i | m_i, \text{EOS}) = \delta(\Lambda_i - \Lambda(m_i; \text{EOS})). \quad (33)$$

This feature enables the possibility to include more physical information on the NS sources during parameter estimation ab initio and can be used through the installation of additional BILBY and PARALLEL BILBY patches that come along with our NMMA framework. Another advantage of this functionality is that information from multiple simulations can be combined to compute a combined posterior because the EOS is a common parameter for all NSs¹⁵⁵.

Combined Sampling. To extract most information from the GW and the EM data, we perform a full parameter estimation combining both likelihoods. The ‘full’ likelihood \mathcal{L} is given by

$$\mathcal{L}(\theta) = \mathcal{L}_{\text{GW}}(\theta_{\text{GW}}) \times \mathcal{L}_{\text{EM}}(\theta_{\text{EM}}), \quad (34)$$

where $\theta = \{\theta_{\text{GW}}, \theta_{\text{EM}}\}$. Because the lightcurve models and the GW waveform models depend on different sets of parameters, simply sampling over all of the parameters would not yield a stronger constraint on the parameters of interest. Therefore, it is key to use connections between different parameters at the prior level. In particular, a few parameters describing the EM signals can be determined by the binary masses and the EOS. For instance, the dynamical ejecta mass $m_{\text{dyn}}^{\text{ej}}$ and the disk mass m_{disk} are connected to the binary properties through the relations discussed in the methods section. The details for all the parameters are summarized in Supplementary Tab. 2.

Table 2 | Posterior of and prior used for the GW170817-and-AT2017gfo and GW170817-and-AT2017gfo-GRB170817A analysis.

Parameter	Name	Connection with other parameters	prior	Posterior
m_i	Component mass	-	$\mathcal{U}(0.5M_\odot, 4.3M_\odot)$	$m_1 = 1.41^{+0.05}_{-0.05} M_\odot$ $m_2 = 1.31^{+0.04}_{-0.04} M_\odot$
EOS	Equation-of-state of nuclear matter	-	$\mathcal{U}(1, 5000)$	EOS = $4734.09^{+253.85}_{-304.07}$
s_i	Component spin	-	Uniform on a sphere with $ s_i < 0.05$	$\mathbf{s}_1 = (0.00^{+0.02}_{-0.02}, 0.00^{+0.02}_{-0.02}, 0.00^{+0.01}_{-0.01})$ $\mathbf{s}_2 = (0.00^{+0.02}_{-0.02}, 0.00^{+0.02}_{-0.02}, 0.00^{+0.01}_{-0.01})$
Λ_i	Tidal deformability	$\Lambda(m_i; \text{EOS})$	-	$\Lambda_1 = 352.71^{+107.84}_{-114.83}$ $\Lambda_2 = 530.26^{+135.03}_{-116.34}$
C_i	Compactness	$C_i = C(m_i; \text{EOS})$	-	$C_1 = 0.17^{+0.01}_{-0.01}$ $C_2 = 0.16^{+0.01}_{-0.01}$
α	Dynamical ejecta mass fitting error	-	$\mathcal{N}(0M_\odot, 0.0004M_\odot)$	$\alpha = -0.00005^{+0.00005}_{-0.00006} M_\odot$
$m_{\text{dyn}}^{\text{ej}}$	Dynamical ejecta mass	$m_{\text{dyn}}^{\text{ej}} = m_{\text{dyn,fit}}^{\text{ej}}(m_i, C_i) + \alpha$	-	$\log_{10}(m_{\text{dyn}}^{\text{ej}}/M_\odot) = -2.25^{+0.10}_{-0.07}$
$M_{\text{threshold}}$	Threshold mass	$M_{\text{threshold}} = M_{\text{threshold}}(\text{EOS})$	-	$M_{\text{threshold}} = 3.76^{+0.10}_{-0.09} M_\odot$
m_{disk}	Disk mass	$m_{\text{disk}} = m_{\text{disk}}(m_i, M_{\text{threshold}})$	-	$\log_{10}(m_{\text{disk}}/M_\odot) = -0.76^{+0.02}_{-0.01}$
ξ	Fraction of the disk mass ejected as wind	-	$\mathcal{U}(0, 1)$	$\xi = 0.61^{+0.18}_{-0.17}$
$m_{\text{wind}}^{\text{ej}}$	Wind ejecta mass	$m_{\text{wind}}^{\text{ej}} = \xi \times m_{\text{disk}}$	-	$\log_{10}(m_{\text{wind}}^{\text{ej}}/M_\odot) = -1.18^{+0.08}_{-0.09}$
Φ	Lanthanide-rich composition opening angle	-	$U(15\text{deg}, 75\text{deg})$	$\Phi = 68.69^{+4.77}_{-4.61} \text{deg}$
ϵ	Fraction of leftover disk mass converted to GRB jet energy	-	$\log \mathcal{U}(-7, -0.3)$	$\epsilon = 0.04^{+0.23}_{-0.04}$
E_0	GRB jet on-axis isotropic energy	$E_0 = \epsilon \times (1 - \xi) \times m_{\text{disk}}$	$\log \mathcal{U}(48, 60)$	$\log_{10}(E_0/\text{erg}) = 51.45^{+1.05}_{-1.24}$
θ_c	Half-width of the jet core	-	$\mathcal{U}(0.01\text{rad}, \pi/2\text{rad})$	$\theta_c = 0.37^{+0.60}_{-0.29} \text{rad}$
θ_w	Truncation angle of the jet	-	$\mathcal{U}(0.01\text{rad}, \pi/2\text{rad})$	$\theta_w = 0.24^{+0.11}_{-0.09} \text{rad}$
n_0	Number density of ISM	-	$\log \mathcal{U}(-6, 0)$	$\log_{10}(n_0/\text{cm}^{-3}) = -3.96^{+1.62}_{-1.73}$
p	Electron distribution power-law index	-	$\mathcal{U}(2, 5)$	$p = 2.11^{+0.07}_{-0.06}$
ϵ_e	Thermal energy fraction in electrons	-	$\log \mathcal{U}(-4, 0)$	$\log_{10} \epsilon_e = -0.77^{+0.77}_{-1.05}$
ϵ_B	Thermal energy fraction in magnetic field	-	$\log \mathcal{U}(-5, 0)$	$\log_{10} \epsilon_B = -2.39^{+2.26}_{-1.64}$
$R_{1.4}$	Radius of a $1.4M_\odot$ neutron star	$R_{1.4}(\text{EOS})$	-	$R_{1.4} = 11.98^{+0.35}_{-0.40} \text{km}$

The table summarizes the intrinsic parameters for the multi-messenger observation of a BNS merger. In the fourth column, we report median posterior values at 90% credibility for the joint inference of GW170817-and-AT2017gfo-and-GRB170817A. $\mathcal{U}(a, b)$ refers to uniform distribution between a and b . $\log \mathcal{U}(a, b)$ refers to the log-uniform (of base 10) distribution, i.e. if $X \sim \log \mathcal{U}(a, b)$, $\log_{10} X \sim \mathcal{U}(a, b)$. $\mathcal{N}(\mu, \sigma)$ refers to a normal distribution with mean μ and variance of σ^2 .

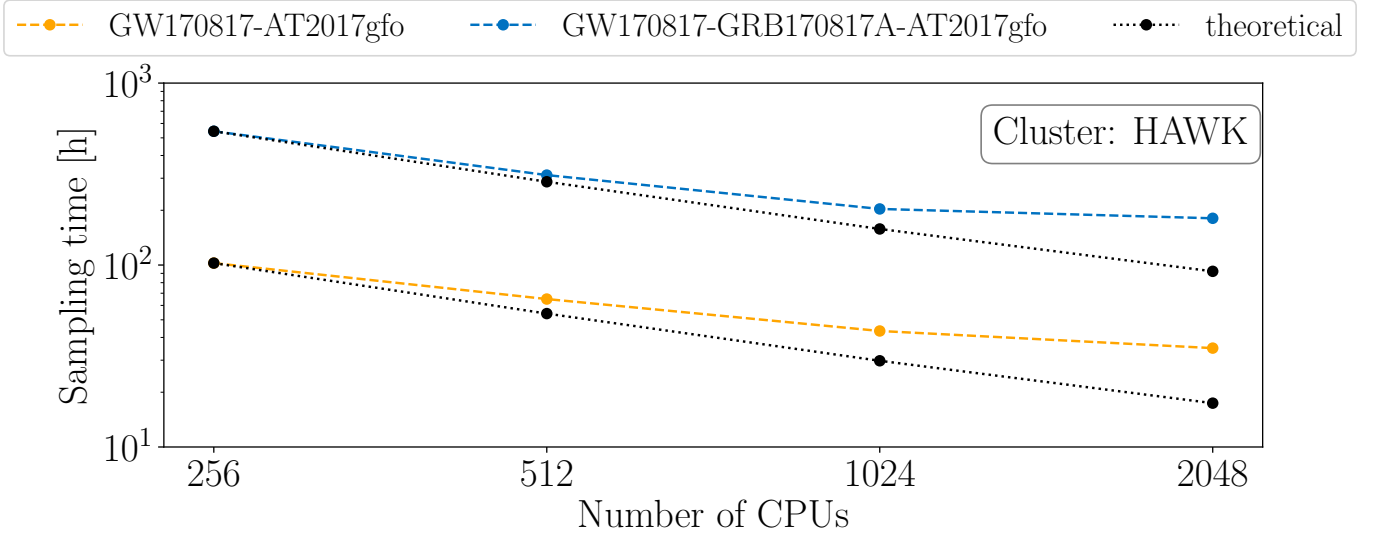


Figure 5 | Scaling performance of the NMMA framework. Theoretical against measured scaling performance for the inference runs of GW170817-AT2017gfo and GW170817-GRB170817A-AT2017gfo on 256, 512, 1024, and 2048 cores, respectively. The theoretical scaling is computed for 256 cores using the reference time $T(N_{\text{core,ref}}) = 102.49 \text{ h}$ for GW170817-AT2017gfo and $T(N_{\text{core,ref}}) = 543.45 \text{ h}$ for GW170817-GRB170817A-AT2017gfo.

Table 3 | Posterior of and prior used for the GW170817-and-AT2017gfo and GW170817-and-AT2017gfo-GRB170817A analysis with the model from Ref. ¹⁵⁴.

Parameter	Name	Connection with other parameters	prior	Posterior
m_i	Component mass	-	$\mathcal{U}(0.5M_\odot, 4.3M_\odot)$	$m_1 = 1.46^{+0.07}_{-0.08} M_\odot$ $m_2 = 1.28^{+0.07}_{-0.06} M_\odot$
EOS	Equation-of-state of nuclear matter	-	$\mathcal{U}(1, 5000)$	EOS = $4686.33^{+289.78}_{-432.21}$
s_i	Component spin	-	Uniform on a sphere with $ s_i < 0.05$	$\mathbf{s}_1 = (0.00^{+0.02}_{-0.02}, 0.00^{+0.02}_{-0.02}, 0.00^{+0.01}_{-0.01})$ $\mathbf{s}_2 = (0.00^{+0.02}_{-0.02}, 0.00^{+0.02}_{-0.02}, 0.00^{+0.01}_{-0.01})$
Λ_i	Tidal deformability	$\Lambda(m_i; \text{EOS})$	-	$\Lambda_1 = 272.25^{+118.90}_{-117.36}$ $\Lambda_2 = 594.23^{+178.28}_{-156.80}$
C_i	Compactness	$C_i = C(m_i; \text{EOS})$	-	$C_1 = 0.18^{+0.01}_{-0.01}$ $C_2 = 0.16^{+0.01}_{-0.01}$
α	Dynamical ejecta mass fitting error	-	$\mathcal{N}(0M_\odot, 0.0004M_\odot)$	$\alpha = -0.00002^{+0.0005}_{-0.0006} M_\odot$
$m_{\text{dyn}}^{\text{ej}}$	Dynamical ejecta mass	$m_{\text{dyn}}^{\text{ej}} = m_{\text{dyn,fit}}^{\text{ej}}(m_i, C_i) + \alpha$	-	$\log_{10}(m_{\text{dyn}}^{\text{ej}}/M_\odot) = -2.17^{+0.16}_{-0.13}$
$M_{\text{threshold}}$	Threshold mass	$M_{\text{threshold}} = M_{\text{threshold}}(\text{EOS})$	-	$M_{\text{threshold}} = 3.05^{+0.08}_{-0.09} M_\odot$
m_{disk}	Disk mass	$m_{\text{disk}} = m_{\text{disk}}(m_i, M_{\text{threshold}})$	-	$\log_{10}(m_{\text{disk}}/M_\odot) = -0.93^{+0.18}_{-0.19}$
ξ	Fraction of the disk mass ejected as wind	-	$\mathcal{U}(0, 1)$	$\xi = 0.26^{+0.13}_{-0.12}$
$m_{\text{wind}}^{\text{ej}}$	Wind ejecta mass	$m_{\text{wind}}^{\text{ej}} = \xi \times m_{\text{disk}}$	-	$\log_{10}(m_{\text{wind}}^{\text{ej}}/M_\odot) = -1.52^{+0.11}_{-0.11}$
$m_{\text{tot}}^{\text{ej}}$	Total ejecta mass	$m_{\text{tot}}^{\text{ej}} = m_{\text{dyn}}^{\text{ej}} + m_{\text{wind}}^{\text{ej}}$	-	$\log_{10}(m_{\text{tot}}^{\text{ej}}/M_\odot) = -1.43^{+0.09}_{-0.09}$
v^{ej}	Ejecta velocity	-	$\log \mathcal{U}(-1, -0.6)$	$\log_{10}(v^{\text{ej}}/c) = -0.74^{+0.06}_{-0.07}$
X_{lan}	Lanthanide mass fraction	-	$\log \mathcal{U}(-5, -2)$	$\log_{10} X_{\text{lan}} = -3.38^{+0.13}_{-0.12}$
ϵ	Fraction of leftover disk mass converted to GRB jet energy	-	$\log \mathcal{U}(-7, -0.3)$	$\epsilon = 0.01^{+0.12}_{-0.01}$
E_0	GRB jet on-axis isotropic energy	$E_0 = \epsilon \times (1 - \xi) \times m_{\text{disk}}$	$\log \mathcal{U}(48, 60)$	$\log_{10}(E_0/\text{erg}) = 51.33^{+1.17}_{-0.99}$
θ_c	Half-width of the jet core	-	$\mathcal{U}(0.01\text{rad}, \pi/2\text{rad})$	$\theta_c = 0.12^{+0.36}_{-0.06} \text{rad}$
θ_w	Truncation angle of the jet	-	$\mathcal{U}(0.01\text{rad}, \pi/2\text{rad})$	$\theta_w = 0.42^{+0.28}_{-0.19} \text{rad}$
n_0	Number density of ISM	-	$\log \mathcal{U}(-6, 0)$	$\log_{10}(n_0/\text{cm}^{-3}) = -2.87^{+1.56}_{-1.53}$
p	Electron distribution power-law index	-	$\mathcal{U}(2, 5)$	$p = 2.11^{+0.06}_{-0.06}$
ϵ_e	Thermal energy fraction in electrons	-	$\log \mathcal{U}(-4, 0)$	$\log_{10} \epsilon_e = -0.61^{+0.61}_{-1.09}$
ϵ_B	Thermal energy fraction in magnetic field	-	$\log \mathcal{U}(-5, 0)$	$\log_{10} \epsilon_B = -2.44^{+1.85}_{-1.9}$
$R_{1.4}$	Radius of a $1.4M_\odot$ neutron star	$R_{1.4}(\text{EOS})$	-	$R_{1.4} = 11.86^{+0.31}_{-0.49} \text{km}$

The table summarizes the intrinsic parameters for the multi-messenger observation of a BNS merger using the kilonova model described in Ref. ¹⁵⁴. In the fourth column, we report median posterior values at 90% credibility for the joint inference of GW170817-and-AT2017gfo-and-GRB170817A. $\mathcal{U}(a, b)$ refers to uniform distribution between a and b . $\log \mathcal{U}(a, b)$ refers to the log-uniform (of base 10) distribution, i.e., if $X \sim \log \mathcal{U}(a, b)$, $\log_{10} X \sim \mathcal{U}(a, b)$. $\mathcal{N}(\mu, \sigma)$ refers to a normal distribution with mean μ and variance of σ^2 .

Scaling. Due to the enormous computational burden of simultaneously analysing both the EM and GW signals, we have to ensure a good parallelization of our code. For the NMMA framework, the parallelization is achieved by taking advantage of the flexibility of `dynesty`¹⁵⁶ and based on the interface presented in `parallelbilby`¹⁵⁷.

In particular, the nested sampling process is parallelized using a head/worker strategy. The “head” organizes the live/dead points, and validates if the stopping criteria are reached, while the “workers” find new live points under the likelihood constraint. The theoretical scaling performance of such a strategy is given by¹⁵⁸

$$T(N_{\text{cores}}) = T(N_{\text{core_ref}}) \times \frac{\ln(1 + N_{\text{core_ref}}/n_{\text{live}})}{\ln(1 + N_{\text{cores}}/n_{\text{live}})}, \quad (35)$$

where $T(N_{\text{cores}})$ is the runtime using N_{cores} cores and $T(N_{\text{core_ref}})$ is the reference time using $N_{\text{core_ref}}$ cores. The parameter n_{live} denotes the number of live points.

To validate if such a scaling is achieved, we performed intensive scaling tests on SuperMUC_NG at the Leibniz Supercomputing Centre (Munich), Lise and Emmy of the North German Supercomputing Alliance, and on HAWK of the High-Performance Computing Center Stuttgart. We show results for scaling tests performed on HAWK using AMD EPYC 7742 processors. The tests are based on a full joint inference of GW170817-and-AT2017gfo and GW170817-and-GRB170817A-and-AT2017gfo which includes intermediate checkpointing and all necessary I/O-operations. The strong scaling for such simulations is shown in Supplementary Fig. 5 and is compared to the theoretical scaling mentioned of Eq. (35).

Modelling Uncertainty. Overall, the obtained multi-messenger constraints depend noticeably on the robustness and accuracy of the individual GW, kilonova, and GRB afterglow models but also on the uncertainty and accuracy of the underlying equations of state and nuclear physics computations. In the past, there have been numerous studies considering the effect of GW-model uncertainties, e.g.,^{155,159,160} and we have already employed multiple GW models in one of our previous studies also to investigate uncertainties with the conclusion that with the current amount of observational data, we are mainly limited by statistical and not systematic uncertainties²². As an example of the influence of the particular choice of the kilonova model, we employ two different kilonova models with different assumptions about the geometry and composition of the ejecta. In particular, we compare the results for our standard kilonova model as presented in Supplementary Tab. 2 with the results based on the model of Kasen et al.¹⁵⁴ in Supplementary Tab. 3. While we find that individual parameters can be different, we find a similar neutron star radius of $R_{1.4} = 11.86^{+0.37}_{-0.49}$ km.

Effect of systematic uncertainty budget To investigate the effect of the value chosen for the systematics uncertainty budget, the analysis on the GW170817-AT2017gfo-GRB170817A event has been conducted with three different values of σ_{sys} , namely, 0.5mag, 1mag and 2mag.

To gauge the effect on the final equation-of-state constraint, the resulting posterior of the radius of a $1.4M_{\odot}$ neutron star, $R_{1.4}$, for these different σ_{sys} are compared. The median values with the 90% credible interval as uncertainties, are shown in Supplementary Tab. 4.

Table 4 | Comparison of radius measurements of a $1.4M_{\odot}$ neutron star for different σ_{sys} .

σ_{sys} [mag]	$R_{1.4}$ [km]
0.5	$12.05^{+0.35}_{-0.45}$
1.0	$11.98^{+0.35}_{-0.40}$
2.0	$11.76^{+0.41}_{-0.49}$

The resulting radius measurements of a $1.4M_{\odot}$ neutron star for σ_{sys} being 0.5, 1.0 and 2.0 are shown.

With lower values of σ_{sys} , the estimated $R_{1.4}$ is skewed towards higher values, with the minimal uncertainty at 1mag. Therefore, it hints that

- the information from difference channels are more coherent at 1mag as compare to 0.5mag
- the information is not over diluted in 1mag as compare to 2mag.

To verify the above claim, we investigate into the estimated best-fit lightcurves. In particular, the best-fit lightcurves with the associated error budget for filter K is shown at Supplementary Fig. 6. One can see that the 0.5mag is underestimating the systematic uncertainty and failed to account for the data after 6 days after the merger, while the 2mag is overcompensating for the systematic uncertainty.

Based on the above observations, we concluded that the σ_{sys} of 1mag is a sensible choice.

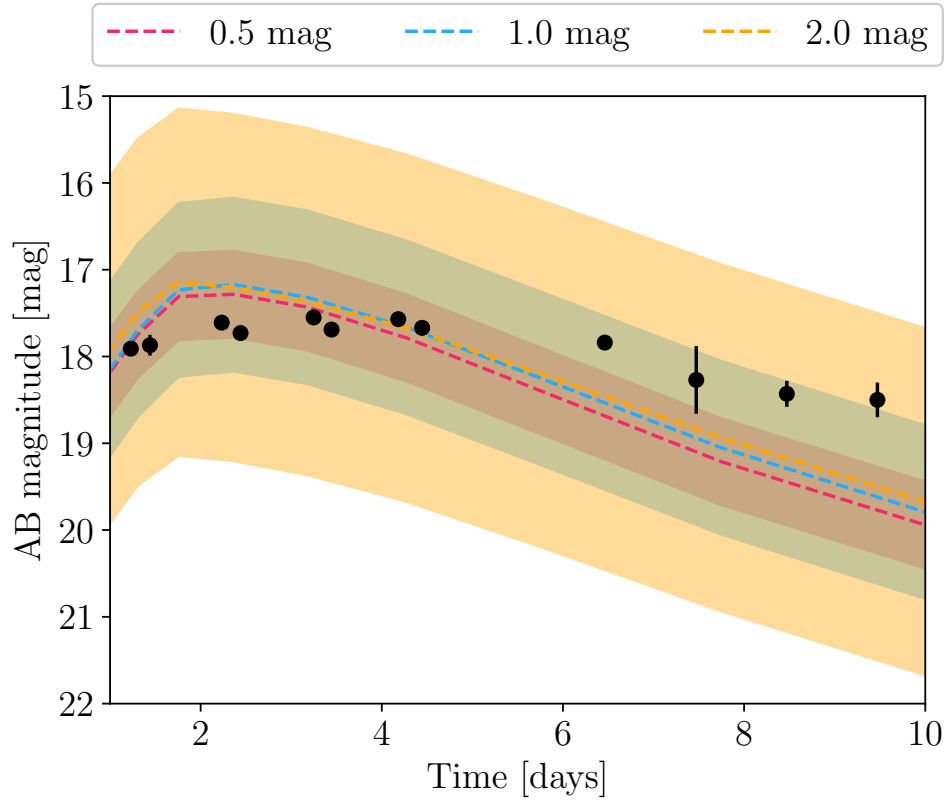


Figure 6 | Best-fit early-time lightcurve from the analysis with various σ_{sys} . The best-fit K-filter lightcurve (dashed, with the one magnitude uncertainty shown as the band) for AT2017gfo data when analysing GW170817-and-AT2017gfo-and-GRB170817A simultaneously with different σ_{sys} .